Journal of Materials Science: Materials in Electronics (2018) 29:20280–20301
https://doi.org/10.1007/s10854-018-0162-2

Carbon-nitride-based core–shell nanomaterials: synthesis and applications

Qiang Guo[1] · Yongli Wan[1] · Bingbing Hu[1] · Xitao Wang[1]

Received: 6 June 2018 / Accepted: 4 October 2018 / Published online: 8 October 2018
© Springer Science+Business Media, LLC, part of Springer Nature 2018

Abstract
As a new type of photo-catalyst, graphitic carbon-nitride-based core–shell nanocomposites (nanomaterial@g-C_3N_4) have shown promising prospect for various applications in the photo-catalysis and other related fields when compared to bare graphitic carbon nitride (g-C_3N_4) due to their unique physicochemical, optical and electrical properties resulting from the synergistic effect between core and shell, and also the protection of g-C_3N_4 shell to inhabit the reaggregation, photo-corrosion, oxidation or dissolution of nanocore. In this review, we have systematically summarized the preparation of g-C_3N_4-based composites, including physical adsorption, hydrothermal growth, thermal vapor condensation and the newly-developed precursor wrapping method according to recent researches. The advantages of g-C_3N_4-based core–shell composites including their physicochemical properties, stability, optical and electronic properties are highlighted. Various applications are addressed, such as photo-catalytic hydrogen production from water splitting, photo-catalytic degradation of organic pollutants, photo-catalytic reduction of carbon dioxide, and photo-electric anti-corrosion. Various strategies for designing and constructing highly effective g-C_3N_4-based core–shell composites are also thoroughly proposed, including band-gap and lattice match, optimization of the preparation method of nanocomposites and nanocore characteristics. This review can provide new directions in exploring g-C_3N_4-based nanomaterials for the applications in photo-catalysis or related fields as well as novel fabrication methods.

1 Introduction

Environmental pollution and energy shortages are two serious problems nowadays that human beings are facing with. Therefore, developing a technology for the production of fuels or valuable chemicals, the degradation of organic pollutants by using solar energy and the conversion of the solar energy into electricity is highly desirable. Photo-catalysis and photo-voltaic system which can achieve the conversion of solar energy into chemical energy, electricity and the elimination of pollutant in water and air have attracted great interests for several decades [1]. Since the 1970s, Fujishima and Honda found the potential application of TiO_2 in photo-catalysis, a large number of semiconductor materials have been designed and used as the photo-catalysts for photo-reduction of CO_2 to useful chemical products such as CH_4, CO, CH_3OH, CH_2O and HCOOH in semiconductor aqueous suspension [2]. In addition, TiO_2 and modified TiO_2, many new non-titanium photo-catalysts were synthesized and showed high photo-catalytic activities. These photo-catalysts include non-TiO_2 metal oxides (ZnO, WO_3, CuO, NiO) [3–7], perovskite-type compound oxides ($SrTiO_3$, $LaCoO_3$) [8, 9], metal sulfides (ZnS, CdS) [10, 11], organic–metallic coordination compounds, and other photo-catalysts (Ag@AgBr/carbon nanotubes, $[Zn_{1.5}Cu_{1.5}\ Ga(OH)_8]_2^+(CO_3)_2{\cdot}mH_2O$ [12–14]). Although many efforts have been taken to improve photo-catalytic performance of photo-catalysts, and considerable advances have been achieved, the disadvantages of some traditional semiconductor materials still impede the development of photo-catalysis due to the relatively large band gap such as ZnO (3.4 eV) or TiO_2 (3.2 eV) only exhibiting photo-activity under UV irradiation, high recombination rate of photo-generated electron–hole pairs [15] and serious photo-corrosion in the long term photo-catalytic processes [16–21] for many photo-catalysts such as ZnO and CdS.

✉ Xitao Wang
wangxt@tju.edu.cn

[1] Collaborative Innovation Center of Chemical Science and Engineering (Tianjin), Tianjin Key Laboratory of Applied Catalysis Science and Technology, College of Chemical Engineering and Technology, Tianjin University, Tianjin 300072, China

Polymeric g-C_3N_4 was firstly reported in 2009 by Wang et al. [22], as a new type of carbon-containing covalent compound photo-catalyst accumulating in the form of graphite-like (2π). Currently, g-C_3N_4 has received increasing attention in the field of photo-catalysis due to its excellent physical stability (up to 600 °C in air), chemical stability (against acid, base, and organic solvent) [23], and its favorable negative conduction band (CB) energy and narrow band gap. Advantages above make g-C_3N_4 a more suitable material for absorbing visible light and performing the reduction of CO_2 and H_2O compared with other photo-catalyst [24–26]. Generally, for photo-catalytic water splitting to H_2, the oxidation potential of photo-catalyst should be more positive than +0.83 V (vs. SHE at pH 7), the reduction potential of the photo-catalyst need to be more negative than −0.413 V (vs. SHE at pH 7) [27]. H_2O is oxidized to O_2 and H^+ by holes in valence band (VB) of photo-catalyst after photo-excitation, H^+ is reduced to H_2 by photo-excited electrons in CB, while for CO_2 reduction, reduction potential of photo-catalyst should be more negative than −0.24 to −0.61 V [28] (vs. SHE at pH 7) corresponding to reduction potential of reducing products (e.g. CH_4 or HCOOH) [28]. In photo-degradation of pollutants such as rhodamine B (RhB) [29–31],methylene blue (MB) [32, 33] and methyl orange(MO) [34, 35], the in-situ generation of hydroxyl radicals and superoxide anion radicals are regarded as main reactive species to oxidize organic pollutants which require the potential of +2.27 V and −0.28 V (vs. SHE at pH 7), respectively. Fortunately, the band gap of pure g-C_3N_4 is 2.7 eV with VB and CB position respectively at ca. 1.6 V and −1.1 V vs. SHE at pH 7. Thus, pure g-C_3N_4 can be an appropriate photo-catalytic material for the applications mentioned above from the perspective of energy level. Furthermore, g-C_3N_4 can be safely synthesized by one-step thermally condensing nitrogen-rich precursors such as melamine [36], dicyandiamide [37], cyanamide [3], urea [38], thiourea [39] and so forth. Up to now, g-C_3N_4 has been widely applied in CO_2 photo-reduction, H_2 generation from photo-catalytic water splitting, super capacitor, wastewater treatment, air purification, photo-current generation [40] and so on. However, bare g-C_3N_4 displays comparatively low photo-activity owing to its small surface area [41], the rapid recombination rate of photo-induced electron–hole pairs, low optical absorption in visible light and low electrical conductivity [42]. Also, high VB position of g-C_3N_4 decreases its photo-catalytic degradation ability and ring opening ability in pollutant elimination such as benzene-based organics [43].

Therefore, pertinence methods are urgently imperative to solve these problems. Recent research progress illustrates the considerable roles of functional modification and heterojunction structure in enhancing photo-activity of carbon nitride [44, 45]. Notably, the carbon-nitride-based core–shell structure is very likely to cope with both drawbacks of traditional semiconductor materials and deficiency of g-C_3N_4 by one step with regard to structure and fast recombination rate of electron and hole pairs. As shown in Scheme 1, g-C_3N_4 is a kind of soft polymer so that it can be facilely coated on the surface of other semiconductors to form core–shell structure [3], which not only hinders the fast recombination of electron–hole pairs due to the formation of heterojunction between "core" and "shell", but also prevents "core" from photo-corrosion, oxidation or dissolution [19, 46]. Compared with pure carbon nitride, inorganic semiconductor@g-C_3N_4 materials actually exhibit excellent photo-activity in the current photo-catalytic applications. This is mainly related to the following reasons. Firstly, conventional semiconductors with large bandgap such as TiO_2 [47], ZnO [48], ZnS [49] and In_2O_3 [50] have inferior photo-catalytic activity under visible light due to their weak response to visible light, while the incorporation of the g-C_3N_4 shell can improve the visible light absorbing performance of photo-catalyst. Furthermore, the coupling effect between shell and core due to the more negative VB and more positive CB of g-C_3N_4 than those of inorganic semiconductors can efficiently promote separation of photo-induced charges, in which the photo-induced electrons (e^-) from g-C_3N_4 shell are transferred to semiconductor core, meanwhile the photo-generated holes (h^+) are moved reversely from semiconductor core to g-C_3N_4 shell.

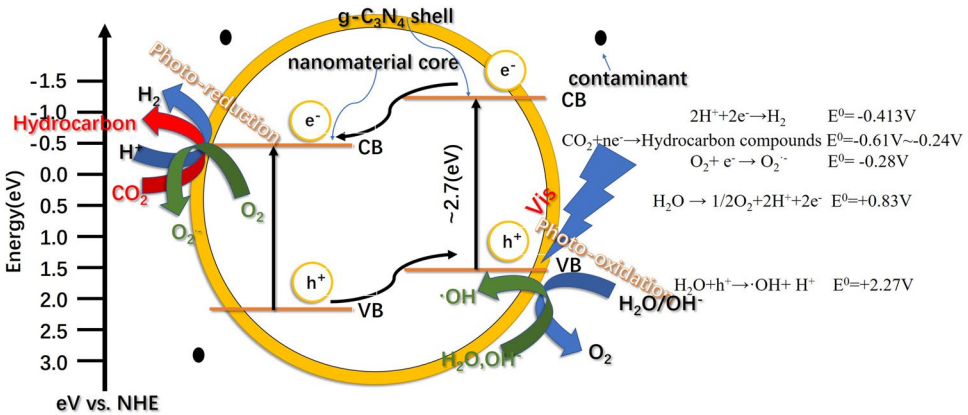

Scheme 1 Schematic diagram of band gap structure and the possible photo-catalytic process of carbon-nitride-based core–shell structured composites

Thus, the activity of core–shell structured materials will be obviously enhanced [51]. As the shell of photo-catalyst, g-C_3N_4 also can resist contaminants, corrosion and dissolution of nanocore in reaction environment owing to its excellent physical and chemical stability.

More importantly, light response to the visible light region for g-C_3N_4 could be enhanced by the formation of core–shell structure and coupling effects between semiconductors and g-C_3N_4. As reported by Pawar et al. [48], apparent red shift of band edge occurred in ZnO/g-C_3N_4 with core–shell structure such as $Z_{0.75}$CN (0.75 wt% zinc source) and $Z_{1.0}$CN (1 wt% zinc source), which indicated the core–shell structure of nanomaterial@g-C_3N_4 probably increased the number of charge carriers of bare g-C_3N_4 under the visible irradiation, leading to superior photo-activity. In addition, g-C_3N_4 shell usually consisting of nanosheets with a thickness of several nanometers displays the vast surface area, which possesses more active centers, better adsorption performance and fast charge transfer capability [52–55].

Within recent 10 years, it is witnessed that relevant publication papers in terms of nanomaterial@g-C_3N_4 with core–shell structure are rising rapidly with time, confirming to the increasing popularity in nanomaterial@g-C_3N_4 as illustrated in Fig. 1. In 2012, composites with core–shell structure between g-C_3N_4 and inorganic semiconductor were reported for the first time in the photo-catalytic field by Pan et al. [56]. They synthesized core–shell structured $BiPO_4$@g-C_3N_4 by facile ultrasonic dispersion method, which displayed significantly enhanced photo-activity. After that, various nanomaterials@g-C_3N_4 photo-catalysts were gradually explored, including metal@g-C_3N_4 [57], metal oxide/phosphide/iodide/sulfide@g-C_3N_4 [58–61], metal–organic framework@g-C_3N_4 [62], inorganic compound@g-C_3N_4 and so on. Besides the development of new g-C_3N_4-based core–shell materials and synthesis methods, the applications of these composites were greatly expanded, such as photo-degradation of pollutants [48], H_2 generation from water splitting [46], CO_2 photo-catalytic or electrocatalytic reduction [58], and photo-electric anti-corrosion [63].

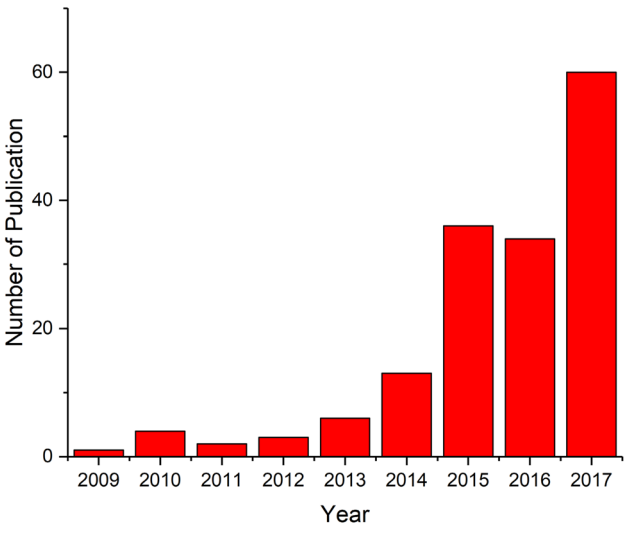

Fig. 1 Evolution of the nanomaterial@g-C_3N_4 composite literatures over 9 years. Source: http://apps.webofknowledge.com; search term: "carbon nitride" OR "C_3N_4" and "core–shell" OR "core/shell"

Even though carbon-nitride-based core–shell structured composites exhibit promising prospect in the photo-catalytic field, relevant and up-to-date review about the synthesis and applications of nanomaterial@g-C_3N_4 photo-catalysts with core–shell structure has not yet to be found so far. Therefore, the present review article mainly presents the synthesis methods, discusses the merit and applied research of g-C_3N_4-based photo-catalysts, and proposes the rational design strategies for g-C_3N_4 core–shell nanomaterials.

2 Preparation of g-C_3N_4-based core–shell nanomaterials

The preparation strategies and conditions have the significant influence on the morphology, phase composition, pore size distribution and specific surface area, chemical and physical properties and photo-electric performances of g-C_3N_4-based core–shell nanomaterials. The fabrication of this kind of material with high efficiency and low cost has always been a challenging task. Currently, there are mainly three technologies to synthesize nanomaterial@g-C_3N_4 core–shell materials, viz physical adsorption, hydrothermal growth and thermal vapor condensation.

2.1 Physical adsorption

Physical adsorption of g-C_3N_4 is the most common method to prepare nanomaterial@g-C_3N_4 photo-catalysts at present owing to its convenience and efficiency. This process consists of three steps as shown in Fig. 2. (1) The preparation of bulk g-C_3N_4 by thermally condensing nitrogen-rich precursors; (2) ultrasonic exfoliation of bulk g-C_3N_4 and centrifugal separation to obtain g-C_3N_4 nanosheets; (3) the preparation of nanomaterial@g-C_3N_4 with core–shell structure by mixing g-C_3N_4 nanosheets and designed nanocore under stirring for a long time to remove the solvent. In this process, g-C_3N_4 nanosheets will spontaneously be coated on the nanocore to achieve the minimum surface energy [3, 56, 62, 64–67]. Among the preparation process above, step (1) and (3) are easy to be achieved, while step (2) is crucial for the preparation of nanomaterial@g-C_3N_4 with proper morphology and photo-electronic property, which require the ultra-thin g-C_3N_4 nanosheets to increase

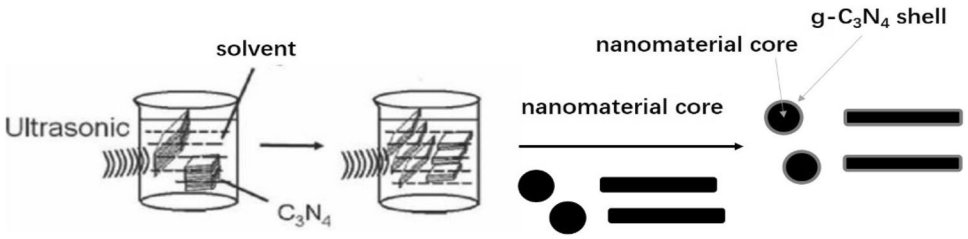

Fig. 2 Schematic illustration of the preparation of the nanomaterial@g-C_3N_4 photo-catalysts. Reprinted from Ref. [56] Copyright 2012, with permission from John Wiley and Sons

the active surface area and enhance the chemical interaction between g-C_3N_4 and nanomaterials.

Generally, the preparation conditions during ultrasonic exfoliation of bulk g-C_3N_4 have the significant influence on the size and thickness of nanosheets, physical and chemical properties, photo-catalytic and electrocatalytic performance. Among these conditions, the solvent effects are widely studied. Deionized water is usually regarded as the best solvent to exfoliate bulk g-C_3N_4 to g-C_3N_4 nanosheets because water has stronger polarity than other solvents such as methanol [66] or ethanol, and thus g-C_3N_4 nanosheets will be exfoliated easily in the deionized water [68]. Additionally, the protonation–exfoliation of g-C_3N_4 with the acid such as H_3PO_4 and HNO_3 can help to exfoliate bulk g-C_3N_4 into 2D ultrathin nanosheets with ample micropores and mesopores and improve its conductivity for charge transportation, resulting in superior photo-catalytic performance [69]. This is because H_3PO_4 can easily intercalate into the layer structure of bulk-g-C_3N_4 due to its selective adsorption to the stranded nitrogen atoms through a Brønsted acid/base interaction. Temperature is another important factor. However, the impacts of temperature in the preparation of nanomaterial@g-C_3N_4 haven't been investigated especially. At present, ultrasonic exfoliation of g-C_3N_4 nanosheets is usually chosen to proceed at room temperature. This can be due to the fact that ambient temperature is pretty easy to control [19, 51]. Predictably, if the solvent is raised to a certain temperature, the increase in temperature may accelerate the peeling of carbon nitride, but the too high temperature may also make peeled g-C_3N_4 nanosheets easy to curl. Consequently, it is difficult to wrap on the semiconductor core.

Although the photo-catalytic efficiency can be further improved via optimizing preparation strategy which can adjust and control the size of g-C_3N_4 nanosheets, the photo-catalytic activity of g-C_3N_4 nanosheets is still too low to meet the requirements for extensive practical applications. Therefore, some synergetic strategies were employed to achieve ultra-thin g-C_3N_4 with unique morphologies, structures and properties, and the further enhanced catalytic performance. These tactics include the fabrication of porous ultrathin nanosheets [70], protonation–exfoliation of g-C_3N_4 [69], O-fictionalization of ultrathin g-C_3N_4 [71], the preparation of fish-scale structured g-C_3N_4 [72], the modification by barbituric acid g-C_3N_4 [67], which are summarized as follows.

2.1.1 Based on mesoporous g-C_3N_4 nanosheets

Compared with nonporous g-C_3N_4 nanosheets, mesoporous g-C_3N_4 (mpg-C_3N_4) nanosheets are considered as a better shell material due to their large surface area. In 2014, Chen et al. [3] synthesized ZnO@*mesoporous*g-C_3N_4 core–shell materials with large surface area via ultrasonic exfoliation of mesoporous g-C_3N_4, in which 12-nm SiO_2 particles were used as the hard template and molten cyanamide as a precursor of g-C_3N_4. Then, the mixture was heated at 90 °C with stirring to evaporate water and calcined at 550 °C for 4 h. Finally, mesoporous g-C_3N_4 was obtained by eliminating the silica template with ammonium bifluoride (NH_4HF_2, 4 M) for 48 h and washing with distilled water and ethanol for 3 times. As a result, mesoporous g-C_3N_4 was easier to be coated on the surface of ZnO and form core–shell structure when compared with nonporous g-C_3N_4 due to a larger number of fragments with the smaller size. This result is ascribed to that the bulk g-C_3N_4 with mesopore possesses more spherical pores, smaller particle density, and larger surface area, which is easier to be peeled off to form g-C_3N_4 nanosheets after ultrasonic vibration. Moreover, the specific surface area of mpg-C_3N_4 is greatly increased beyond 162 m^2/g, which reveals that ZnO@mpg-C_3N_4 may exhibit better photo-catalytic activity due to a large number of reactive sites compared with ZnO@*nonporous*g-C_3N_4. Also, In_2O_3@mpg-C_3N_4 [51] and AgI@mpg-C_3N_4 [61] core–shell nanomaterials were also prepared by the same method and exhibited the improved photo-catalytic activities due to the more homogeneous core–shell structure and the larger specific surface area resulting from the introduction of mesoporous g-C_3N_4 shell.

In order to further increase the photo-catalytic performance of g-C_3N_4-based core–shell materials, the combination of mesoporous preparation and heteroatom doping such as O, P is used to alter the surface properties, electric conductivity and photo-absorption of g-C_3N_4. Phosphorus was reported to be an ideal dopant as phosphorus doped g-C_3N_4 (P-C_3N_4) can improve the separation of photo-induced hole-electron pairs, thus improving the photo-catalytic activity [70]. Chen et al. prepared bulk P-doped C_3N_4 through

thermal polycondensation of a mixture of melamine and hexachlorotriphosphazene, and then mesoporous P-C_3N_4 ultrathin nanosheets were obtained from bulk P-doped C_3N_4 above through frozen expansion and post-thermal exfoliation. Subsequently, P-C_3N_4/$ZnIn_2S_4$ nanocomposites were fabricated through electrostatic attraction between Zn^{2+} and In^{3+} on the surface of the P-C_3N_4 ultrathin nanosheets. 20 wt% P-C_3N_4/$ZnIn_2S_4$ sample exhibited the highest photo-catalytic activity under visible light irradiation, which was almost 5 times higher than that of pure P-C_3N_4 and about 3 times higher than that of $ZnIn_2S_4$. The enhanced photo-catalytic performance is mainly related to the efficient separation of photo-induced charge carriers due to the coupling effect between P-C_3N_4 and $ZnIn_2S_4$.

Oxygen is considered as the important dopant as well because O-g-C_3N_4 can facilitate the formation of core–shell structure based on C–O–C groups and extend the range of light absorption. ZnO/O-g-C_3N_4 was synthesized by the Xing et al. [71] through physical adsorption. g-C_3N_4 nanosheets were oxidized by hydrogen peroxide through the hydrothermal process, which was accompanied simultaneously by ZnO nanoparticles dispersed in deionized water. It is found that introduced oxygenous groups confirmed by XPS analysis in O-g-C_3N_4 are helpful to form the ZnO/O-g-C_3N_4 with core–shell structure. More importantly, ZnO/O-g-C_3N_4 remarkably enhanced photo-catalytic activity compared with ZnO, g-C_3N_4 nanosheets, and ZnO/g-C_3N_4 samples because of blocking the recombination rate of electron and hole pairs effectively. Up to now, g-C_3N_4 nanosheets doped by other nonmetal elements (e.g., B, F, or S) have not been investigated completely. Possibly, it can be taken as a promising way to enhance the photo-catalytic activity of nanomaterials@g-C_3N_4 in the near future.

2.1.2 Based on fish-scale structured g-C_3N_4 nanosheet

It is a fascinating protocol to design and construct nanostructures by mimicking the various structures in nature for obtaining the productions with the desired properties. It is reported that a unique fish-scale structure possesses many advantages owing to its inimitable properties. Firstly, a great number of pores are introduced in the fish-scale structured materials, which increase the optical absorption active sites to efficiently capture photons and absorb sunlight. Secondly, the spatial arrangement of the fish-scale flakes can multiple scatter and reflect light and prolong the light residence time and enhance the light harvesting efficiency. Finally, photo-generated charges separation efficiency can be improved remarkably since the photo-generated electrons can be selectively transferred from fish-scale flat to the edges of fish-scale flakes. Lin et al. [72] synthesized fish-scale structured g-C_3N_4 nanosheets by solvothermal treatment of the mixture of g-C_3N_4 nanosheets, PVP and hexadecyl trimethyl ammonium in ethanediol solution at different temperatures for 6 h. The as-prepared fish-scale structured g-C_3N_4 nanosheets had higher H_2 evolution rate of 1316.4 μmol $h^{-1}g^{-1}$ when compared with common g-C_3N_4 nanosheets. Although the core–shell materials have not been reported at present based on fish-scale structured g-C_3N_4, it is predicted that relevant photo-catalyst with core–shell structure would be synthesized soon due to outstanding properties in fish-scale structured g-C_3N_4.

2.1.3 Based on g-C_3N_4 nanosheets modified by barbituric acid

Zhang et al. [67] reported the preparation of core–shell CdS@g-C_3N_4 nanowires through physical adsorption, in which the appropriate amount of barbituric acid was used to incorporate plentiful carbon atoms into the nitrogen sites of g-C_3N_4. Then, g-C_3N_4 nanosheets modified by barbituric acid were obtained through liquid ultrasonically exfoliating. The results showed that the partial substitution of N by C in g-C_3N_4 nanosheets could apparently expand the visible responsive range of g-C_3N_4 and improve the photo-catalytic performance of CdS@g-C_3N_4.

Similarly, various core–shell nanomaterials including Bi_2WO_6@g-C_3N_4 [64], Ag_3PO_4@g-C_3N_4 [65], Cu_2O@g-C_3N_4 [59, 73], $CuFe_2O_4$@g-C_3N_4 [66], $BiPO_4$@g-C_3N_4 [56], TiO_2*hollow-microsphere*@g-C_3N_4 [74] and etc. are also synthesized by physical adsorption. As revealed, the formation of core–shell structure is one of the most effective approaches to improve the photo-catalytic performance of semiconductors due to the enhancement of photo-absorption and the strong electric field at the interface near the band-edge offset, which can significantly speed up the transfer and separation of photo-generated charge carriers.

In addition to the preparation of mononuclear carbon-nitride-based core–shell nanomaterials using physical adsorption method, dual-core or multi-core catalysts can also be obtained by this preparation method, which opens up a new gate for the improvement of photo-catalytic efficiency. Singh et al. [75] synthesized successfully g-C_3N_4/a-TiO_2/c-TiO_2 with core–shell structured photo-catalyst through the process as illustrated in Fig. 3. The pristine TiO_2 (c-TiO_2) was prepared by sol–gel method and partially reduced with hydrogen to form a-TiO_2/c-TiO_2 core–shell particles. Actually, a-TiO_2 formed on the surface of c-TiO_2 has much lower bandgap than c-TiO_2, thus increasing the light absorption of the as-prepared sample. Especially, the efficient separation of electrons and holes can be achieved by a-TiO_2/c-TiO_2 with core–shell structure because of the Schottky barrier at the interface of a-TiO_2 and c-TiO_2. After the coat of g-C_3N_4 nanosheets, the photo-induced electrons can be transferred directly

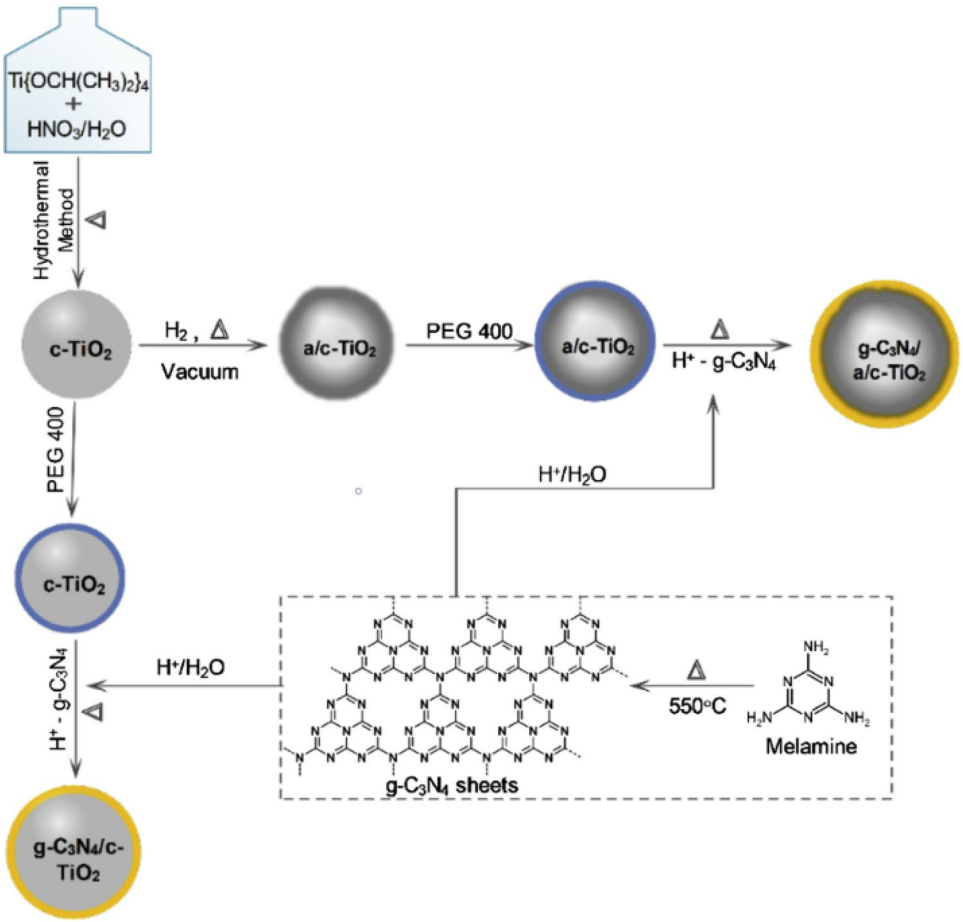

Fig. 3 Schematic illustration for the preparation of g-C_3N_4/a-TiO_2/c-TiO_2 heterostructure nano-catalyst. Reprinted from Ref. [75] Copyright 2016, with permission from Elsevier

from g-C_3N_4 to c-TiO_2 through a-TiO_2 due to the tight interfacial connections. Reversely, as shown in Fig. 4b, holes can be migrated to g-C_3N_4 from c-TiO_2 due to the suitable CB and VB levels of them. Briefly, improved photo-activity is due to the increased light absorption in the visible region and efficient charge separation as a result of effective interfacial electron transfer between g-C_3N_4, a-TiO_2, and c-TiO_2 in the g-C_3N_4/a-TiO_2/c-TiO_2 composite.

2.2 Hydrothermal growth

Hydrothermal growth method usually involves the in-situ formation of the nanocore and coating for g-C_3N_4 nanosheets on the nanocore. During the preparation, the as-prepared g-C_3N_4 ultrathin nanosheets are dispersed in different precursor solutions of the core, and then core nanomaterials are formed under the g-C_3N_4 layer due to the combination of anions and cations or chemical reaction under hydrothermal conditions, and nanomaterial@g-C_3N_4 with core–shell structure is further achieved. By this preparation method, a

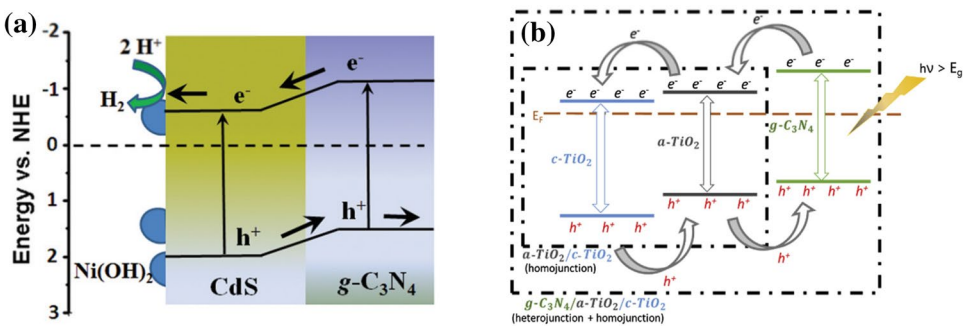

Fig. 4 **a** The photo-catalytic mechanism of Ni(OH)$_2$–CdS/g-C_3N_4 samples under visible light irradiation. Reprinted from Ref. [91] Copyright 2016, with permission from Royal Society of Chemistry; **b** proposed schematic for the energy band structure of g-C_3N_4/a-TiO_2/c-TiO_2. Reprinted from Ref. [75] Copyright 2016, with permission from Elsevier

strong chemical interaction between the g-C_3N_4 shell and core can be produced. As a result, the g-C_3N_4 shell is probably distributed more stably and uniformly on the surface of the core semiconductor.

Li et al. [58] prepared successfully $LaPO_4$@*tube*g-C_3N_4 with core–shell structure via the hydrothermal growth method. It is demonstrated that $La^{3+}$and $PO4^{3-}$ went inside in g-C_3N_4 and grew along the tube wall due to the hydrothermal growth and $LaPO_4$@*tube*g-C_3N_4 with well-defined nanorod morphology of $LaPO_4$ was inherited as shown in Fig. 5. Similarly, ZnO@g-C_3N_4 with core–shell structure was prepared through the hydrothermal growth method by Pawar et al. [48]. Actually, there is a slight change in the morphology of g-C_3N_4 and ZnO particles instead of nanorods because of the different loading amount of ZnO on g-C_3N_4.

O-functional g-C_3N_4 was utilized to prepare core–shell nanomaterials through hydrothermal growth. Wang et al. [76] synthesized O-functional g-C_3N_4 through intercalation and exfoliation of the obtained bulk g-C_3N_4. They used the mixture of $NaNO_3$, $KMnO_4$, H_2SO_4 (98%, wt%) and H_2O_2 to oxidize bulk g-C_3N_4 to O-functional g-C_3N_4. Subsequently, Cu foils were oxidized by a solution containing O-functional g-C_3N_4 to Cu_2O. Meanwhile, reduced g-C_3N_4 spontaneously coated on generated Cu_2O to form Cu_2O@g-C_3N_4 core–shell nanowires with highly hierarchical sharp edges as shown in Fig. 6 to achieve the steady-state. Actually, Cu_2O@g-C_3N_4 core–shell nanowire displays better in current density and

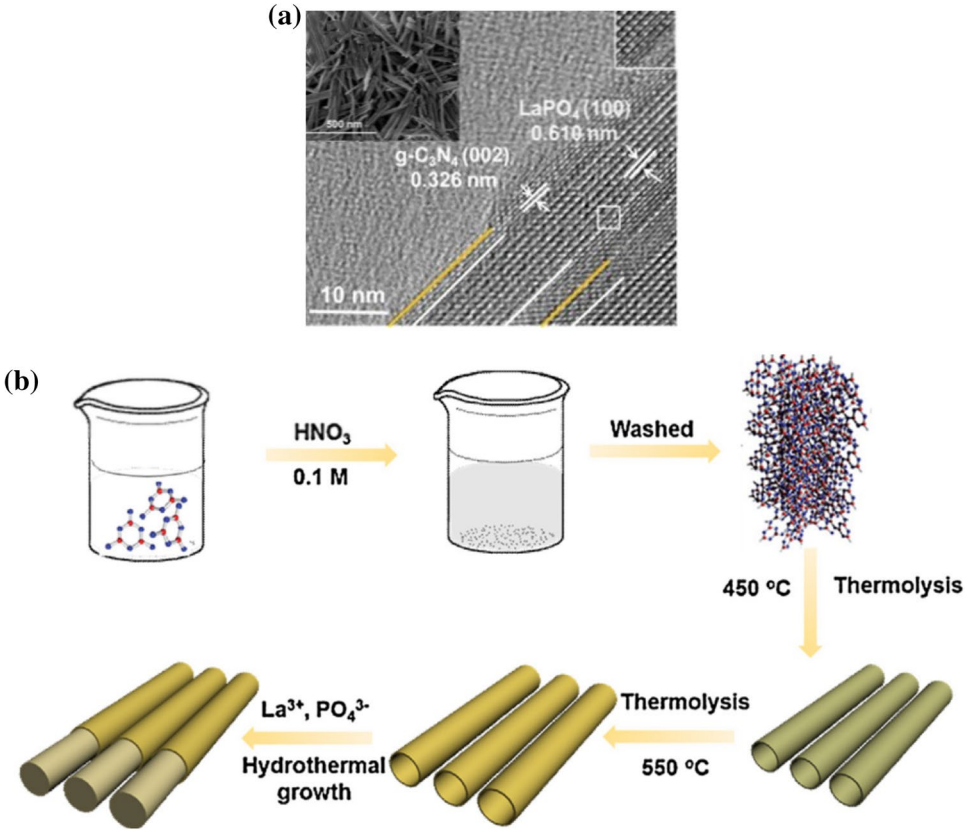

Fig. 5 **a** TEM and SEM images of $LaPO_4$@*tube*g-C_3N_4; **b** schematic illustration of the synthesis of the core–shell $LaPO_4$@*tube*g-C_3N_4 nanocomposites. Reprinted from Ref. [58] Copyright 2017, with permission from Elsevier

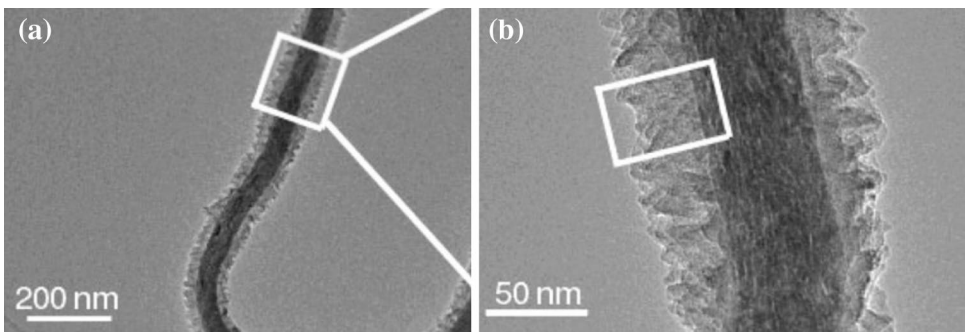

Fig. 6 TEM image of the prepared Cu_2O–g-C_3N_4 core–shell nanowires. Reprinted from Ref. [76] Copyright 2015, with permission from Royal Society of Chemistry

EIS measurements by contrast with a mixture of Cu_2O and g-C_3N_4 due to the synergetic interaction of the Cu_2O and g-C_3N_4.

Combinational photo-catalyst (Ag_3PO_4/$BiPO_4$@MIL-88B(Fe)@g-$C_3N_{4)}$ with the core–shell structure to take advantages of MOF and g-C_3N_4, as well as Ag_3PO_4/$BiPO_4$ oxy-acid composites was firstly synthesized by Sepideh et al. [77]. The mixture of $FeCl_3{\cdot}6H_2O$ and H_2BDC in DMF was added to the solution containing dispersed g-C_3N_4 nanosheets before being heated at 110 °C for 24 h. Then, as the substrate of the Ag_3PO_4/$BiPO_4$@MIL-88B(Fe)@g-C_3N_4, brown MIL-88B(Fe)@g-C_3N_4 can be collected after drying. Ag_3PO_4/$BiPO_4$ was deposited on the MIL-88B(Fe)@g-C_3N_4 through the hydrothermal method. Due to the formation of heterojunction by coupling Ag_3PO_4/$BiPO_4$, MIL-88B and g-C_3N_4 components, high visible light absorption ability and rapid transportation and mobility of photo-generated electrons in the specific p-conjugated networks of the MIL-88B(Fe)@g-C_3N_4 facilitate the separation of photo-excited electron and hole pairs and hinder recombination of the charge carriers.

2.3 Thermal vapor condensation

For thermal vapor condensation method, the as-prepared nanocore and g-C_3N_4 precursor are sintered together in the covered alumina crucible at high temperature (usually 550 °C) for 2–3 h. The thermal vapor of g-C_3N_4 precursor usually tends to polymerize and condense on the surface of nanocore to form the "shell" layer. Although this method is the most convenient to prepare nanomaterial@g-C_3N_4 photo-catalysts for all three methods, the loading amount and distribution of g-C_3N_4 are quite hard to be controlled. Additionally, the g-C_3N_4 precursor is essential for the successful preparation of core–shell materials, in which strong sublimation and polymerization of the precursor at about 500 °C are required. Melamine is one of the most suitable precursors often used in the preparation of g-C_3N_4 shell [57, 78].

Park et al. [78] reported the synthesis of vertically aligned ZnO nanorods on the FTO substrate glass plate. The shell of g-C_3N_4 on ZnO nanorods was loaded by thermal vapor condensation method. The detailed preparation process is shown in Fig. 7. Similarly, urea and CdS nanorods grown on FTO glass were used to prepare CdS*nanorods*@g-C_3N_4 with core–shell structure via thermal vapor condensation by Li et al. [60]. Lin et al. [79] chose cyanamide as the precursor of photo-catalyst to prepare SiO_2@g-C_3N_4 by thermal vaporization condensation under nitrogen protection. In this process, the cyanamide and SiO_2 nanospheres were kept together at 70 °C for 2 h so that the molten cyanamide can contact the SiO_2 particles sufficiently. After being cooled to ambient temperature, the obtained-product was ground and then heated at 550 °C for 4 h to fabricate SiO_2@g-C_3N_4 with core–shell structure. For these materials, the presence of HI-type hysteresis loop as illustrated in the Fig. 8a confirmed the presence of voids in the core–shell structure and interstitial holes in the core–shell nanospheres. All the samples showed the increase in BET specific surface area when compared with the pristine g-C_3N_4. There are two possible reasons to explain this phenomenon. Firstly, the formation of core–shell structure would allow g-C_3N_4 to be well dispersed on the surface of silica nanospheres and make the shell of g-C_3N_4 thinner, leading to the increase of the specific surface area. Secondly, cyanamide loaded on the silica surface can gradually be polymerized into dicyandiamide, melamine, and g-C_3N_4 at the high temperature as shown in Fig. 8b thus producing more pores inside of g-C_3N_4, eventually, resulting in an increase in specific surface area. Zhang et al. [80] obtained ZnS@g-C_3N_4 using thiourea and zinc nitrate by one-step calcination. It is noteworthy that thiourea is both sulfur source of ZnS and precursor of g-C_3N_4, so the method provides a convenient and straightforward way for the preparation of core–shell structured sulfide.

In addition to the formation of g-C_3N_4, the precursor of g-C_3N_4 can also be used as a reducing agent to reduce metal oxide in this method [57]. Duanet et al. [57] reported the preparation of Co@g-C_3N_4-rGO with core–shell structure using melamine and Co_3O_4 nanoparticles through thermal vapor condensation as illustrated in Fig. 9. Interestingly, melamine plays two crucial roles in this preparation: (1) reducing agent, which can reduce Co_3O_4 nanoparticles to Co metal; (2) precursor of carbon nitride, which can wrap on the surface of Co particles to form shell layer.

Although the methods above have been widely used to prepare various g-C_3N_4 based core–shell nanomaterials with improved photo-catalytic activities, obvious drawbacks still exist for these methods such as larger layer

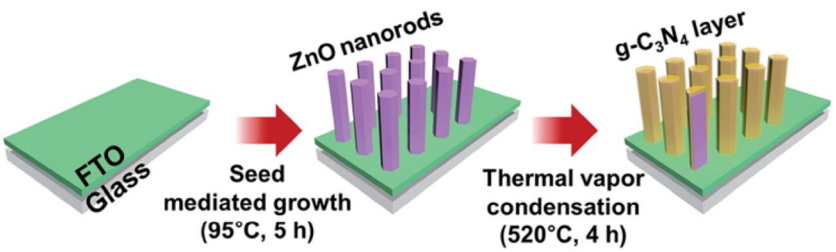

Fig. 7 Schematic illustration of the fabrication process of zinc oxide (ZnO) with g-C_3N_4 films on the fluorine-doped tin oxide (FTO)-coated glass substrate. Reprinted from Ref. [78] Copyright 2016, with permission from Royal Society of Chemistry

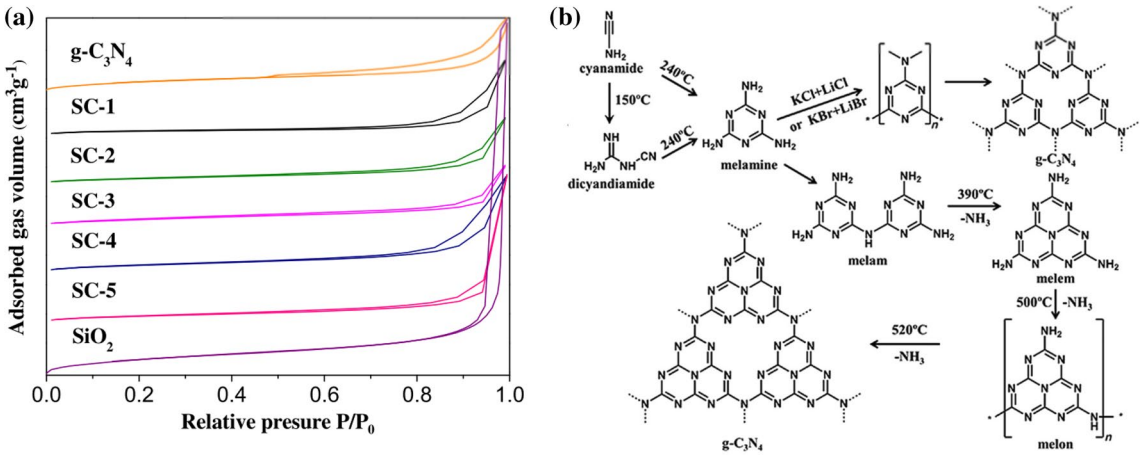

Fig. 8 **a** Nitrogen adsorption–desorption isotherms of pure g-C_3N_4, SiO_2 nanospheres and the SiO_2/g-C_3N_4 core–shell nanospheres. Reprinted from Ref. [79] Copyright 2015, with permission from Elsevier; **b** thermal polymerization pathways of g-C_3N_4. Reprinted from Ref. [42] Copyright 2015, with permission from John Wiley and Sons

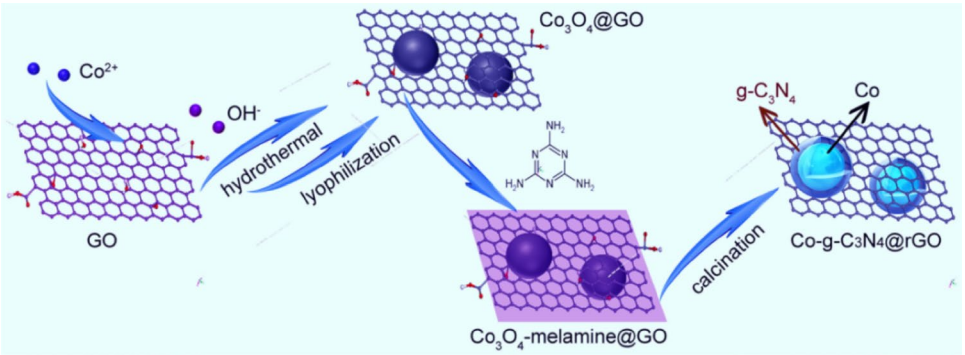

Fig. 9 Schematic illustration of structural evolution processes from precursors to Co@g-C_3N_4-rGO. Reprinted with permission from Ref. [57] Copyright 2016, American Chemical Society

thickness, uncontrollable loading amount and distribution of g-C_3N_4 on the surface of the core and weak chemical interaction between core and shell. To overcome these problems, a new method for preparing nanomaterial@g-C_3N_4 photo-catalysts, called precursor wrapping method, is developed as shown in Fig. 10. For this new method, the precursor of g-C_3N_4 is used to wrap thoroughly the nanocore, and then the as-prepared sample is calcined at the proper temperature to obtain nanomaterial@g-C_3N_4 photocatalysts. This method is a simple and feasible strategy to prepare g-C_3N_4-based core–shell nanomaterials with strong chemical interaction between core and shell, much thinner shell thickness, well dispersion of g-C_3N_4 on the shell and controllable loading amount of g-C_3N_4. Among the many g-C_3N_4 precursors, cyanamide is most suitable precursor due to its excellent solubility in water and its availability to achieve g-C_3N_4 with various morphologies depending on different templating agent [81–83]. During the preparation using this method, adsorption of the g-C_3N_4 precursor on nanocore is the key for core–shell nanomaterials for superior performance. It is preferable that the nanomaterial core carries the acidic group such as aluminium oxide and silicon oxide containing the hydroxyl group, which can react with the amino group in cyanamide. Acidic functional group of nanocore can be obtained through acidification process. In addition, the rough surface and larger surface area of the nanocore can increase the residence time of the cyanamide on the surface of nanocore, which favors the adsorption of cyanamide on the surface of nanomaterial core. The temperature of cyanamide also has the significant influence on the adsorption of cyanamide. It is because that there is indeed the direct relationship between the temperature and viscosity in the most of liquid, and the high viscosity may result in better "sticking" performance of cyanamide liquid. Therefore, it is predicted that the appropriate nanomaterial cores should have the following characteristics: abundant acid groups, rough surface structure (large specific surface area) and proper particle diameter (400–700 nm). As indicated in Fig. 10, when the particle size of nanocore is relatively small, the cyanamide intends to wrap more nanocores to form the "raisin bread model", and the g-C_3N_4 with

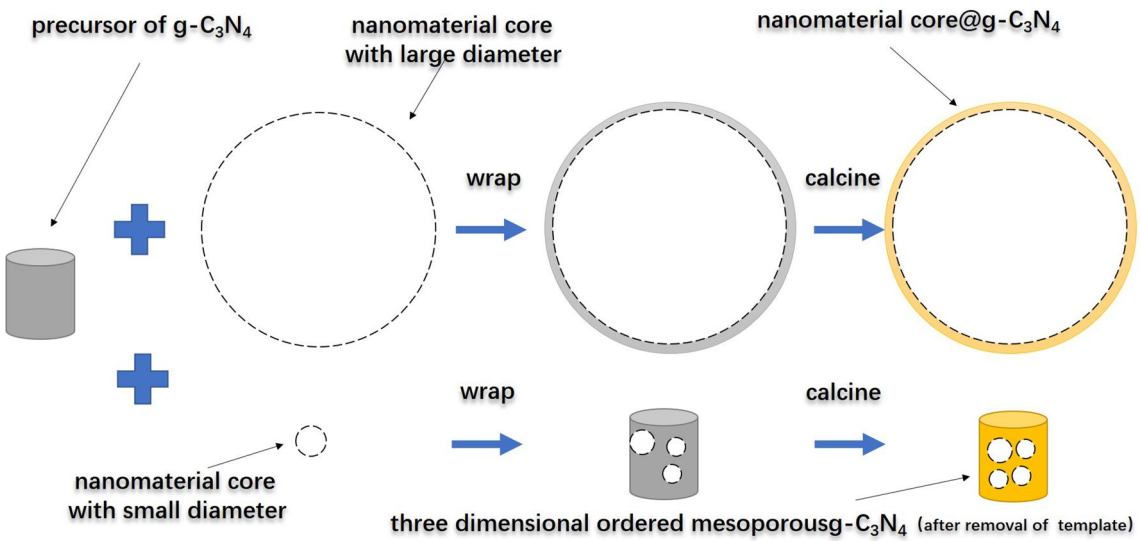

Fig. 10 Schematic illustration of preparation about nanomaterial@g-C_3N_4 photo-catalysts via wrapping method

three-dimensional ordered mesoporous structure can be obtained on removal of nanocore particles. In contrast, single nanocore with large diameter could be easily wrapped by the cyanamide resulting in the formation of hollow spherical g-C_3N_4 after removal of the nanomaterial core. In summary, nanomaterial core wrapped by cyanamide can be obtained in cyanamide aqueous solution where the appropriate nanomaterial core is dispersed evenly. Consequently, nanomaterial@g-C_3N_4 with core–shell structure can be achieved via thermal polycondensation of cyanamide.

3 The application of nanomaterial@g-C_3N_4

As a metal-free and visible-light-responsive photo-catalyst, g-C_3N_4 has become a new hotspot and drawn many attentions in the arena of photo-catalysis because of its suitable electronic band structure, high physicochemical stability, and "earth-abundant" nature. However, bare g-C_3N_4 exhibits inferior photo-catalytic activity owing to its low visible light absorption and fast recombination of photo-generated carriers. A common method to improve the performance of bare g-C_3N_4 is to modify the g-C_3N_4 with another semiconductor or metal which possesses well-matched energy levels to form heterojunction nanostructures, especially composites with core–shell structure that exhibits obvious advantages. Up to now, diverse nanomaterial@g-C_3N_4 with core–shell structure have been synthesized using different core types such as metal [57], metal oxide/phosphide/iodide/sulfide [58–61, 84], metal–organic framework [62, 77], inorganic compound [85] and so on. The nanomaterial@g-C_3N_4 is used in many different fields as shown in Table 1.

3.1 Photo-catalytic hydrogen production from water splitting

g-C_3N_4 has been widely used for photo-catalytic hydrogen production due to its favorable negative CB and narrow band gap energy, which make it become a more suitable semiconductor for absorbing visible light and performing the reduction of protons (H^+) during the water splitting when compared with other semiconductors. It has been reported that the photo-catalytic activity of g-C_3N_4 for H_2 evolution from water splitting can be enhanced remarkably by the formation of core–shell structure based-g-C_3N_4 with a proper nanocore. For example, Bai et al. [46] have reported significantly higher photo-catalytic activity for hydrogen evolution reaction using Ag@g-C_3N_4 when compared with g-C_3N_4 due to the plasma resonance effect and the formation of a heterogeneous structure between Ag and g-C_3N_4. Under the irradiation of visible light, electrons can be stimulated from VB of g-C_3N_4 to CB of g-C_3N_4 and then captured by the Ag core, which would improve the separation of photo-generated carriers. Also, the formation of core–shell of Ag@g-C_3N_4 improves the visible light absorption capacity of g-C_3N_4. Furthermore, the core–shell structure of Ag@g-C_3N_4 cannot only prohibit the re-aggregation of Ag particles through isolation by the g-C_3N_4 shell but also the corrosion and dissolution problems resulting from excessive contact between Ag particles and reactants. Thus, the photo-catalytic stability of the materials is also improved owing to the formation of the core–shell structure. Like Ag@g-C_3N_4 photo-catalyst, the Co@g-C_3N_4-rGO, a core–shell structured

Table 1 Important application of nanomaterial@g-C_3N_4 photo-catalysts

Catalyst (nanomaterial@g-C_3N_4)	Preparation method	Optimal mass or mass fraction(g-C_3N_4)	Main application	References
Cu_2O*nanowire*@g-C_3N_4	HTG	–	–	[76]
Cu_2O*octahedron*@g-C_3N_4	PA	5%	HG	[73]
Cu_2O*nanosphere*@g-C_3N_4	PA	5%	HG	[59]
$CuFe_2O_4$@C_3N_4	PA	~33%	PD (Orange II)	[66]
TiO_2@C_3N_4	MM	5%	PD (MB)	[86]
TiO_2*nanorod*@C_3N_4	TVC	–	PE	[87]
TiO_2*hollow-microsphere*@g-C_3N_4	PA	15%	PD (RhB)	[74]
C-TiO_2@C_3N_4	TVC	–	HG	[88]
(a-TiO_2@c-TiO_2)@g-C_3N_4	PA	4%	PD (MB) & HG	[75]
ZnS@g-C_3N_4	TVC	–	HG & PD (RhB)	[80]
ZnO@C_3N_4	MM	5%	PD (MB)	[89]
ZnO@g-C_3N_4	PA	4%	PD (MB)	[3]
ZnO@g-C_3N_4	HTG	25%	PD (RhB)	[48]
ZnO@g-C_3N_4	PA	1%	PEA	[63]
N-ZnO@g-C_3N_4	PA	5%	PD (RhB)	[19]
ZnO*nanorod*@g-C_3N_4	TVC	–	PD (MB)	[78]
ZnO@O-g-C_3N_4	PA	20%	PD (RhB& Phenol)	[71]
CdS@g-C_3N_4	PA	3%	HG	[90]
CdS*nanowire*@g-C_3N_4	PA	2%	HG	[67]
CdS*nanorod*@g-C_3N_4	TVC	–	HG	[60]
$Ni(OH)_2$–CdS@g-C_3N_4	PA	4%	HG	[91]
$LaPO_4$@g-C_3N_4	HTG	200 mg	PR (CO_2)	[58]
In_2O_3@C_3N_4	PA	3%	PEA	[51]
WO_3@g-C_3N_4	PA	1%	PD(RhB)	[92]
SnO_2@g-C_3N_4	TVC	–	PD (MO)	[34]
Si*nanowire*@g-C_3N_4	TVC	90 µL	HG	[93]
SiO_2@g-C_3N_4	TVC	–	PD (RhB)	[79]
carbon@g-C_3N_4	PA	500 mg	HG	[94]
Ag@C_3N_4	PA	99.5% & 90%	PD (MB) & HG	[46]
AgI@g-C_3N_4	PA	5%	PD (MB)	[61]
Ag_3PO_4@g-C_3N_4	PA	7%	PD (MB)	[65]
$AgFeO_2$@g-C_3N_4	PA	20%	PD (Acid red G&HCHO)	[95]
Bi_2WO_6@g-C_3N_4	PA	3%	PD (MB, RhB, MO and phenol)	[64]
Beta-Bi_2O_3@g-C_3N_4	PA	5%	PD (tetracycline)	[96]
$BiPO_4$@C_3N_4	PA	4%	PD (MB)	[56]
$BiVO_4$@g-C_3N_4	PA	7%	PD(RhB)	[97]
Co@g-C_3N_4-rGO	TVC	–	HG	[57]
N-doped $CsTi_2NbO_7$@g-C_3N_4	TVC	–	PD (RhB)	[98]
Ag_3PO_4/$BiPO_4$@MIL-88B(Fe)@g-C_3N_4	HTG	30 mg	PD (AB92)	[77]

TVC thermal vapor condensation (including in-situ growth), *PA* physical adsorption, *HTG* hydrothermal growth, *MM* mechanical milling, *HG* hydrogen generation, *PD* photo-degradation; *PEA* photo-electrochemical anti-corrosion, *PE* photo-electrochemical, *PR* photo-catalytic reduction, *AB92* navy acid blue 92; g-C_3N_4 and C_3N_4 are almost the same in the table above

photo-catalyst, prepared by Duan et al. [57] showed excellent catalytic activity in hydrogen production from $NaBH_4$ and NH_3BH_3 hydrolysis. Wherein the core Co metal provides not only a catalytically active site but also a magnetic source to achieve a synergistic effect. Furthermore, g-C_3N_4 shell prevents Co nanoparticles from aggregation and growth and also strengthens the contact between graphene oxide (GO) and Co to prevent them from being washed away. The photo-catalytic hydrogen production rate of ZnS@g-C_3N_4 under visible light irradiation was found to be 6 times higher (11.85 µmol/4 h) than that of pure ZnS, which is attributed to the formation of core shell structure and the improvement

of the separation efficiency of photo-generated charge carriers [80].

It was investigated by Liu et al. [73] that the recombination rate of photo-generated electron–hole pairs for octahedron Cu_2O@g-C_3N_4 decreased obviously when compared with single Cu_2O or g-C_3N_4 due to the synergistic effect of the heterojunction between Cu_2O and g-C_3N_4. According to the experimental analysis, Cu_2O@g-C_3N_4 containing 5% wt g-C_3N_4 nanosheets showed the highest hydrogen production rate (795 μmol/g/3 h) among Cu_2O@g-C_3N_4 with other mass fraction of g-C_3N_4 nanosheets. Interestingly, g-C_3N_4 nanosheets adsorbed on the surface of Cu_2O enhance the quick transfer of photo-generated electrons from Cu_2O to g-C_3N_4 nanosheets, thus achieving efficient separation of photo-generated electrons and holes. At the same time, the core–shell structure retards the photo-corrosion of Cu_2O, resulting in the increased stability of Cu_2O@g-C_3N_4 during the photo-catalytic hydrogen production. Similarly, nanospherical Cu_2O@g-C_3N_4 with the g-C_3N_4 loading of 5 wt% (CN5) also displayed good photo-catalytic hydrogen production rate (606.86 μmol/g in 3 h), compared with that of pure Cu_2O or g-C_3N_4, respectively [59]. Also, the effects of exposed crystal faces of octahedral Cu_2O on the photo-catalytic activity were investigated as shown in Fig. 11. It was found that the octahedral Cu_2O with more exposed (111) plane exhibited higher photo-catalytic activity than Cu_2O nanospheres. Therefore, the control of the morphology and the exposed crystal faces of the catalyst is an important way to enhance the activity of the catalyst [73].

Zhang et al. [67] prepared CdS*nanowire*@g-C_3N_4 with different g-C_3N_4 content, and found that CdS*nanowire*@g-C_3N_4 containing 2 wt% of g-C_3N_4 showed the best photo-catalytic hydrogen-production rate, which can reach 4152 μmol/h/g under visible light illumination because of synergic effect between g-C_3N_4 and CdS nanowires, leading to an effective separation of the photo-generated charge. This is because photo-induced electrons (e^-) from the g-C_3N_4 shell can be transferred to CdS nanowires. Meanwhile, the photo-generated holes (h^+) are moved reversely from CdS nanowires to the g-C_3N_4 shell, and photo-generated electrons and holes can be separated immediately in the presence of visible light illumination. Furthermore, core–shell structure of CdS*nanowires*@g-C_3N_4 substantially reinforces photo-stability of CdS nanowires even in a non-sacrificial system by preventing CdS from the photo-corrosion by holes. Recently, photo-catalyst with multiple components was reported by Yan et al. [91]. They have successfully fabricated $Ni(OH)_2$-CdS@g-C_3N_4 with hetero-structure nanowires through ultrasonic exfoliation and physical adsorption with $Ni(OH)_2$ (hydrothermal method), which was used as a highly efficient photo-catalyst for visible light-driven hydrogen production from water spitting. Due to the rapid transfer of photo-generated charge carriers among g-C_3N_4, CdS and $Ni(OH)_2$, the recombination rate of the photo-generated electron and hole pairs decreased significantly, resulting in improved photo-catalytic activity when compared with the single component catalyst. The maximum hydrogen production rate of $Ni(OH)_2$-CdS@g-C_3N_4 was 115.18 μmol/h/mg, ~26 times better than that of CdS*nanorod*/g-C_3N_4 composite and ~7 times higher than that of 0.5 wt% Pt–CdS*nanorod*/g-C_3N_4 composite. More importantly, the activity of the photo-catalyst remained almost unchanged after continuous reaction for 40 h because of the existence of g-C_3N_4 shell which inhibited the photo-corrosion of CdS as illustrated in Fig. 4.

3.2 Photo-catalytic degradation of the organic substance

Nanomaterial@g-C_3N_4 with core–shell structure has also been employed in the photo-catalytic decomposition of organic pollutants such as methylene blue, rhodamine B, aromatic compounds and so on. As the main reactive

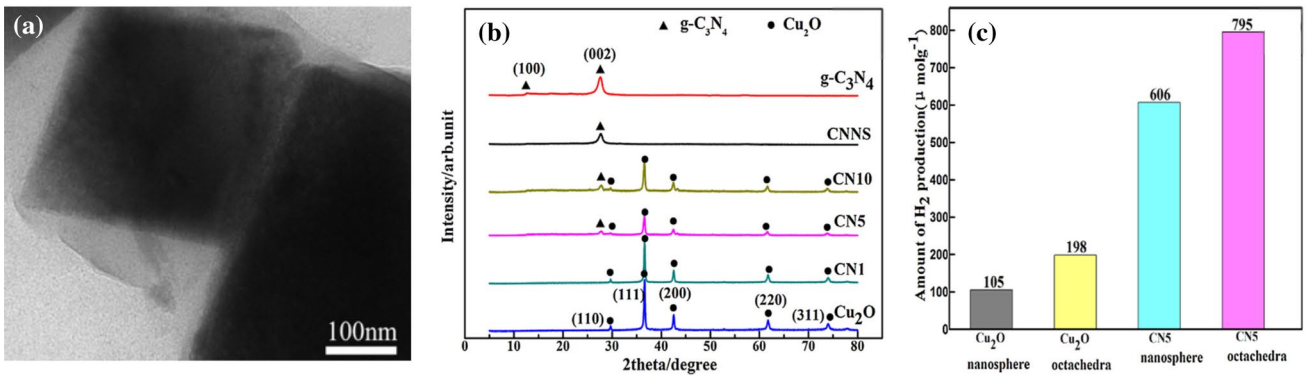

Fig. 11 **a** TEM images of CN5; **b** XRD patterns of g-C_3N_4, g-C_3N_4 nanosheets, Cu_2O, Cu_2O@g-C_3N_4 photo-catalysts; **c** contrast experiments of Cu_2O nanosphere, Cu_2O octahedral, CN5 nanosphere and CN5 octahedra under visible light irradiation for 3 h. Reprinted from Ref. [73] Copyright 2015, with permission from Elsevier

species to oxidize organic contaminants, hydroxyl radicals and superoxide anion radicals can be promoted in the nanomaterial@g-C_3N_4 photo-catalysts due to the core–shell structure. The relevant cases are introduced as below.

Among various photo-catalysts based g-C_3N_4, ZnO@g-C_3N_4 is used widely in the photo-catalytic removal of organic pollutants. Pawar et al. [48] found that the degradation rate of RhB over ZnO*nanoparticle*@g-C_3N_4 prepared by hydrothermal growth method was about 2 times higher than that of pure g-C_3N_4, and about 6 times higher than that of pristine ZnO. While the degradation rate of ZnO*nanorod*@g-C_3N_4 synthesized by Park et al. [78] via thermal vapor condensation method was around 20 times higher than that of pure nanorod ZnO. Moreover, it can be observed from Fig. 12c that the visible light absorption of ZnO@g-C_3N_4 is extended, which is assigned to the synergistic effect in the intimate contact area between ZnO and g-C_3N_4. The better photo-stability in cyclic runs for both photo-catalysts above can be achieved owing to the protection of shell of g-C_3N_4 [48]. TiO_2@g-C_3N_4 exhibits the same trend as ZnO@g-C_3N_4 during the photo-catalytic degradation of RhB [86].

Because of the larger surface area containing more reactive sites, mpg-C_3N_4 is also introduced as the shell to enhance the photo-activity. Chen et al. [3] synthesized ZnO@mpg-C_3N_4 with various loading content of mpg-C_3N_4 and found that the visible light absorption ability of ZnO@mpg-C_3N_4 can be improved with the increase of the mass fraction of mesoporous carbon nitride. The photo-catalytic activity of ZnO@mpg-C_3N_4 with 20 wt% mpg-C_3N_4 for degrading MB was 5.0 times higher than that of normal mpg-C_3N_4 under visible light irradiation. The increase in photo-catalytic performance under the visible light is attributed to the high separation and facile transfer of photo-generated electron–hole pairs at the heterojunction interfaces, which is possibly resulted from the match of the lattice and energy level between the mpg-C_3N_4 shell and ZnO core. This is because mpg-C_3N_4 usually presents

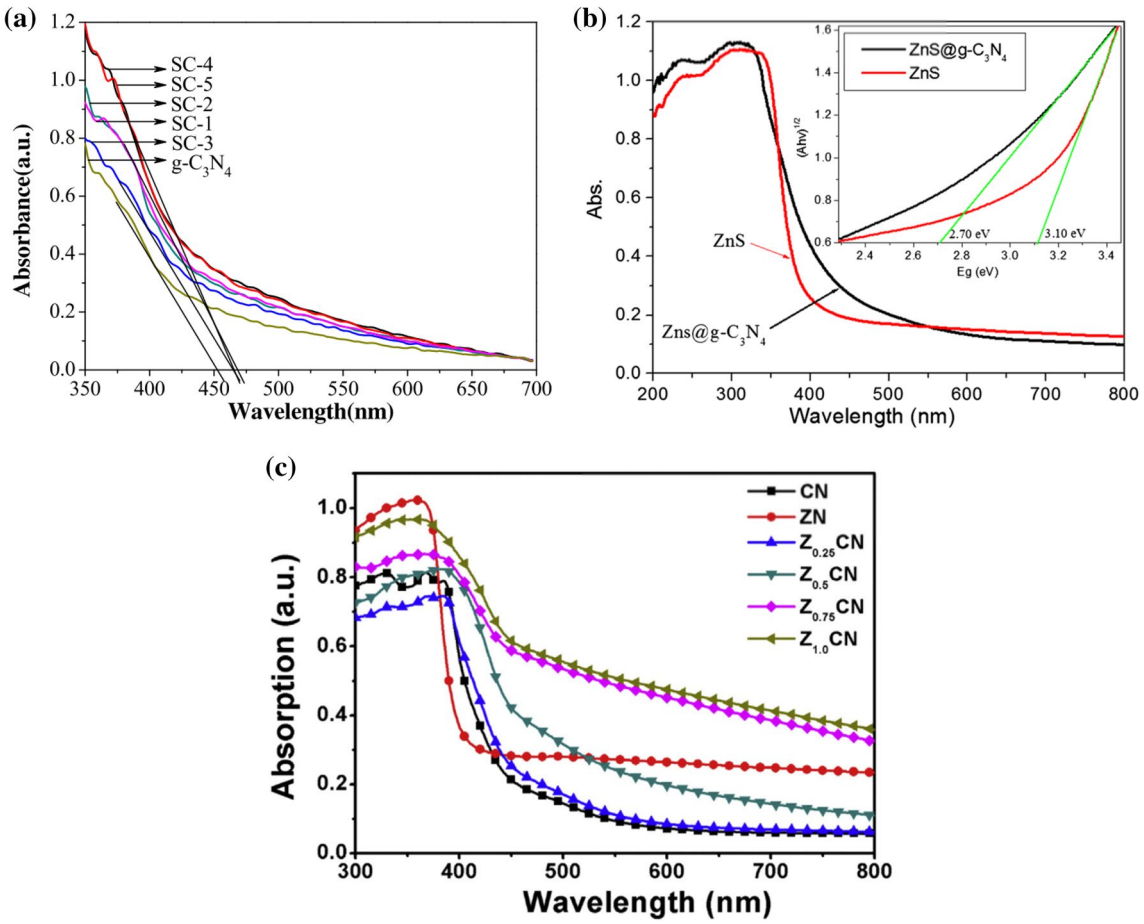

Fig. 12 **a** UV–Vis diffuse reflectance spectra of pure g-C_3N_4 and the SiO_2@g-C_3N_4. Reprinted from Ref. [79] Copyright 2015, with permission from Elsevier; **b** DRS spectra of the bulk ZnS and ZnS@g-C_3N_4. Reprinted from Ref. [80] Copyright 2015, with permission from John Wiley and Sons; **c** DRS spectra of ZnO@g-C_3N_4, ZnO and g-C_3N_4. Reprinted from Ref. [48] Copyright 2016, with permission from Elsevier

(002) crystal face, meanwhile the (002) crystal face on the surface of ZnO is generally found. So, similar crystal face may make them contact each other tightly through adsorption force and result in the decrease of electrical resistance at the heterojunction interfaces. Besides, the position of energy levels of mpg-C_3N_4 and ZnO core are well-matched. It means that the reverse transfer of electrons and holes can readily occur. Thus, effective separation and facile transfer of photo-induced electron–hole pairs leading to the high photo-activity can be achieved.

The photo-catalytic activity of ZnO@g-C_3N_4 can be enhanced by the modification of ZnO with N-doping (N-ZnO@g-C_3N_4). Kumar et al. [19] have proved that the nitrogen atom introduced in ZnO acts as a trap to capture electrons, and decreases the recombination rate of photo-generated electron and hole pairs in N-ZnO@g-C_3N_4, resulting in improved photo-catalytic activity for the degradation of RhB. In addition, the transfer of electrons from N-ZnO to g-C_3N_4 due to the formation of heterojunctions between the g-C_3N_4 and N-ZnO is proved to follow the Z-scheme route as shown in Fig. 13b [99–101], but not the two-way transfer route shown in Fig. 13a. This is because that the position of CB of N-ZnO is much lower than the energy level of O_2^-/O_2 and the position of VB of g-C_3N_4 is much higher than the energy level of $OH^{\cdot}/H_2O$, the oxidation and reduction reaction cannot occur. However, the experimental results show that N-ZnO@g-C_3N_4 does have the good activity in photo-degradation of RhB. So, the authors have sensible assumptions that the route of the electrons transfer conforms to the Z-scheme route. In Z-scheme route, photo-generated electrons would transfer to VB of g-C_3N_4 from the CB of N-ZnO. Thus, the separation ability of the electron–hole pairs of the N-ZnO@g-C_3N_4 is enhanced, and the photo-generated electrons by the Z-scheme transfer route increase the redox capacity of the photo-catalysts as well as the degradation activity for RhB due to low CB potential of g-C_3N_4 which is able to produce $^{\cdot}O_2^-$. Furthermore, N-ZnO@g-C_3N_4 was able to achieve 90% of the original photo-catalytic activity after 6 runs because of the introduction of the core–shell structure, thus improving the susceptibility of N-ZnO to light.

ZnS@g-C_3N_4 has also been employed successfully in degradation of RhB in aqueous solution under visible light [80]. It is proved that the photo-catalytic activity of the ZnS@g-C_3N_4 composite was better than that of single ZnS or g-C_3N_4, and RhB was almost entirely degraded after 4 h as illustrated in Fig. 12a. Besides the reduction in recombination rate of photo-induced electrons and holes, the enhanced light absorption of the composite samples is another reason for higher photo-catalytic activity as observed in Fig. 12b. Due to the narrowed band gap and the change of electronic structure after g-C_3N_4 incorporation, more electrons and holes are produced under the visible-light irradiation. Furthermore, ZnS@g-C_3N_4 keeps comparatively stable during the photo-catalytic oxidation of the pollutant molecules depending on the protection of g-C_3N_4. Actually, the photo-catalytic efficiency of the ZnS@g-C_3N_4 composite descends only 7% after 4 cycles.

Lin et al. [79] synthesized the SiO_2@g-C_3N_4 with core–shell nanospheres structure. Owing to the defects and vacancies on the silica surface, the photo-catalytic performance of SiO_2@g-C_3N_4 increased drastically. Authors found that the addition of SiO_2 inhibits the recombination of photo-generated electron–hole pairs since surface defects and vacancies on the surface of silica can capture photo-generated electrons, thus improving the separation efficiency of photo-generated electrons and holes. When the mass ratio of SiO_2 to cyanamide was 1.5/1, the sample exhibited the highest photo-catalytic activity, and 94.3% of RhB can be degraded after 150 min compared with the ordinary g-C_3N_4 or other counterparts under visible light. Furthermore, the experimental data proves that the core–shell structure has

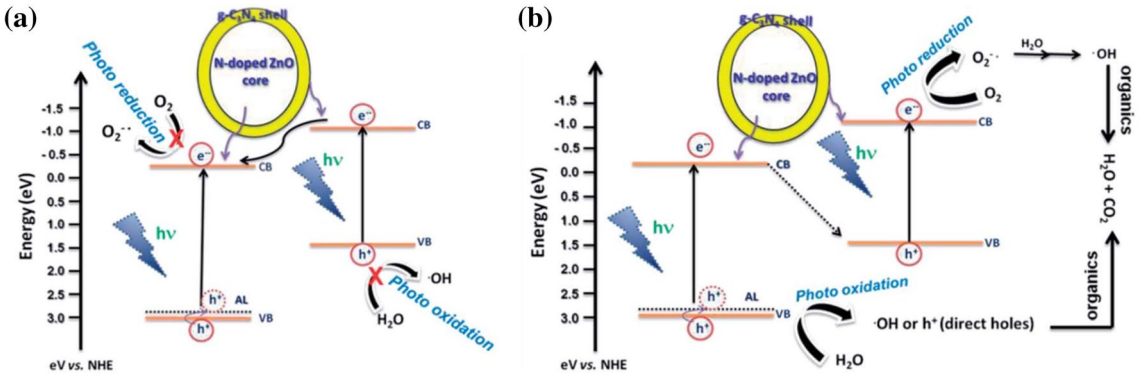

Fig. 13 Schematic diagram showing the mechanism for photo-induced charge carrier transfer in the most conventional composites (not Z-scheme photo-catalysts) (**a**) and N-doped ZnO@g-C_3N_4 (Z-scheme photo-catalysts) (**b**) under visible-light irradiation. Reprinted from Ref. [19] Copyright 2014, with permission from Royal Society of Chemistry

a positive impact on the visible light absorption of photo-catalysts as shown in Fig. 12a.

The (a-TiO_2@c-TiO_2)@g-C_3N_4 is a more effective photo-catalyst for pollutant degradation (MB) when compared with c-TiO_2@g-C_3N_4, a-TiO_2@c-TiO_2 and pristine of g-C_3N_4 and a-TiO_2. This is because the photo-generated electrons of g-C_3N_4 directionally migrate to c-TiO_2 through a-TiO_2 due to the close interfacial connections between a-TiO_2@c-TiO_2 and g-C_3N_4. Subsequently, the more efficient separation of photo-induced electron–hole pairs can be achieved in space as illustrated in Fig. 4b.

Ag and its compounds usually perform better capacity in photo-catalytic degradation of organic materials. However, their photo-catalytic stability is rather weak because of aggregation and photo-corrosion of Ag nanoparticles. Coupling Ag nanoparticles with g-C_3N_4 to form core–shell composites can improve its stability remarkably. On the one hand, the heterojunction structure of core–shell nanomaterials such as Ag@g-C_3N_4 can promote separation of photo-induced electrons and holes; On the other hand, the shell can protect silver compounds from being excessively reduced to the metal. Bai et al. [46] reported that when the weight ratio of Ag was 0.5%, Ag@g-C_3N_4 exhibited the best photo-catalytic activity in the degradation of MB. As electron capturer, Ag captured electrons from the CB of g-C_3N_4, resulting in the reduction of electron–hole recombination, while photo-generated electrons and holes continued to be involved in the redox reaction to photo-degrade MB. Ag@g-C_3N_4 with Ag content of 0.5 wt% also exhibited excellent photo-catalytic stability for photo-degrading MB. After irradiation of 48 h, the catalyst still maintained a photo-catalytic activity beyond 95% of that for the fresh one.

Similarly, AgI@g-C_3N_4 at a weight ratio of 5% (g-C_3N_4/Ag) prepared by Liu et al. [61], used in photo-catalytic degradation of MB, exhibited the best photo-degradation ability in comparison with pure g-C_3N_4 and AgI component. Enhanced separation capacity of photo-generated electron and hole pairs is attributed to the heterojunction caused by core–shell structure between AgI and g-C_3N_4. Meanwhile, AgI@g-C_3N_4 exhibited better photo-catalytic stability during the photo-catalytic degradation.

The Ag_3PO_4@g-C_3N_4 with the content of 7.0 wt% g-C_3N_4 composite prepared by Liu et al. [65] presented the best photo-catalytic activity, photo-degrading 97% MB and 94.6% bisphenol A (BPA) respectively after irradiation for 30 min. Superior photo-stability and photo-activity are also observed in the cyclic runs and crystalline structures as proved by XRD patterns and XPS spectra as shown in Fig. 14, respectively. Wherein no noticeable change in Ag_3PO_4@g-C_3N_4 before and after the reaction is observed. Well-aligned band-structures and the strong interaction in the intimate contact interface improve charge separation, resulting in excellent photo-catalytic activity.

When the mass ratio of g-C_3N_4:$BiPO_4$ reached 10% (CNBP-10), $BiPO_4$@g-C_3N_4 prepared by Pan et al. [56] exhibited the highest photo-catalytic activity for degrading MB by 85% in 6 h in comparison with pure g-C_3N_4 or $BiPO_4$ or other $BiPO_4$@g-C_3N_4 at the different mass ratio of g-C_3N_4:$BiPO_4$. It is proved that core–shell structure plays a relatively important role in decreasing the recombination rate of photo-induced electrons and holes at heterojunction interfaces and enhancement in visible light absorption. More importantly, the synergetic effect can be strengthened due to the lattice match between g-C_3N_4

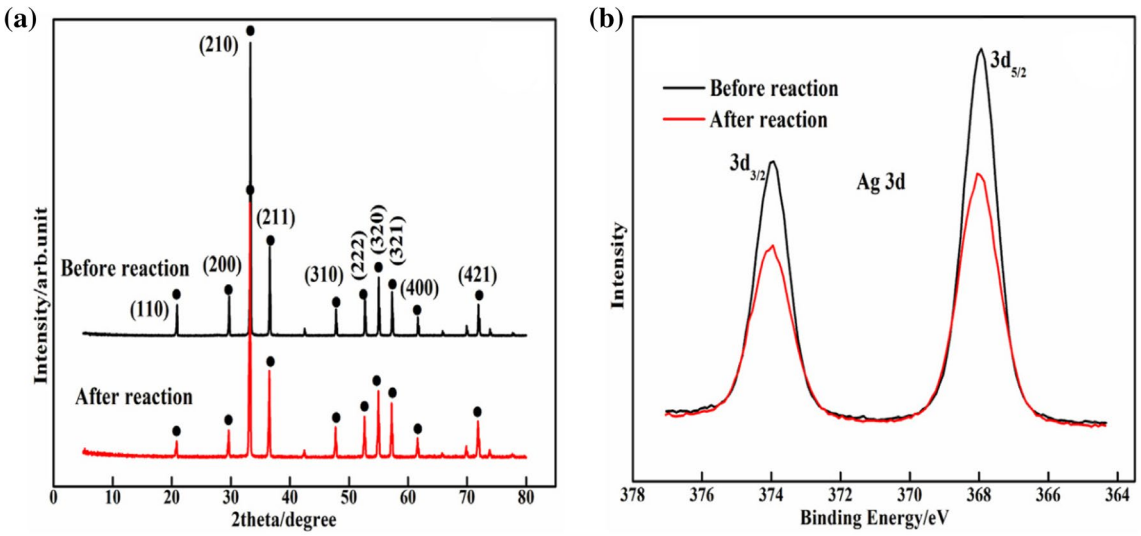

Fig. 14 **a** XRD of before and after the reaction in Ag_3PO_4@g-C_3N_4; **b** Ag 3d XPS spectra before and after the photo-catalytic reaction. Reprinted from Ref. [65] Copyright 2016, with permission from Elsevier

and $BiPO_4$ according to the TEM and XRD results as observed in below Scheme 2, and the formation of the core–shell structure may be induced by lattice match.

Bi_2WO_6@g-C_3N_4 photo-catalyst exhibited unexceptionable photo-catalytic activity in photo-degradation of MB, RhB, and MO compared with the single component semiconductors because of the longer lifetime of electron–hole pairs caused by the synergistic effect in the heterojunction interface. As observed in Fig. 15a under visible irradiation, the Bi_2WO_6@g-C_3N_4 shows the highest current density among Bi_2WO_6, g-C_3N_4, and Bi_2WO_6@g-C_3N_4. Efficient separation of photo-generated electron–hole pairs is proved by transient photo-current. From Fig. 15b, Nyquist plots diameter of Bi_2WO_6@g-C_3N_4 manifests much smaller value over pristine Bi_2WO_6 and g-C_3N_4. Therefore, lower resistance and the faster interfacial charge transfer are affirmed by electrochemical impedance spectroscopy [64].

3.3 Photo-electric anti-corrosion

Corrosion of metal is a widespread natural phenomenon, it is not only causing substantial economic losses but also creates serious environmental pollution. It has been reported that composite photo-catalysts with based-g-C_3N_4 core–shell structure can be used in the photo-electrochemical protection of metal cathodes. Among them, the potential application prospect of ZnO@g-C_3N_4 [63]. And In_2O_3@g-C_3N_4 [51] have been proved owing to their fast electron transfer ability and suitable band gap position in the anti-corrosion of steel.

In 2014, Bu and et al. [63] found that ZnO@g-C_3N_4 obtained through physical adsorption method had good photo-electrochemical corrosion resistance. ZnO@g-C_3N_4 composite flakes with mass fraction of g-C_3N_4/ZnO = 1% achieved the excellent photo-electrochemical anti-corrosion capability for 304 stainless steel, which was due the fact that the ZnO@g-C_3N_4 composite photo-electrode exhibits a maximum visible light induced current density and the minimum photo-generated electrons transfer resistance compared with

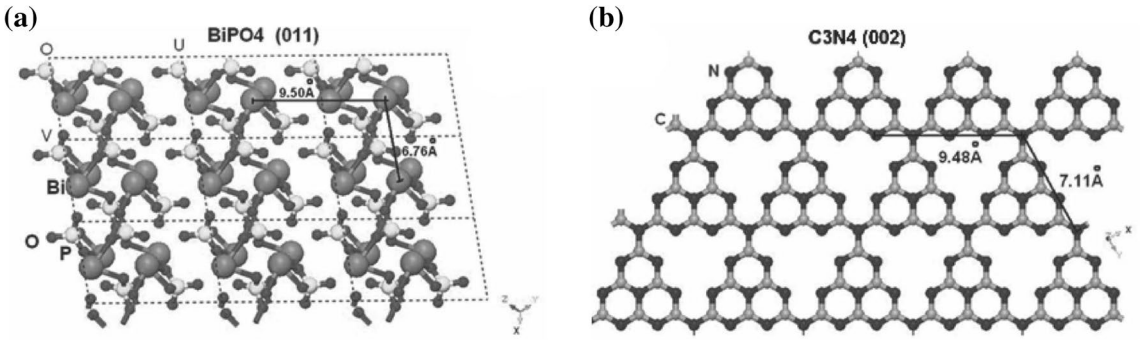

Scheme 2 Schematic illustration of the lattice match between **a** (011) surface of $BiPO_4$ and **b** (002) surface of g-C_3N_4. Reprinted from Ref. [56] Copyright 2012, with permission from John Wiley and Sons

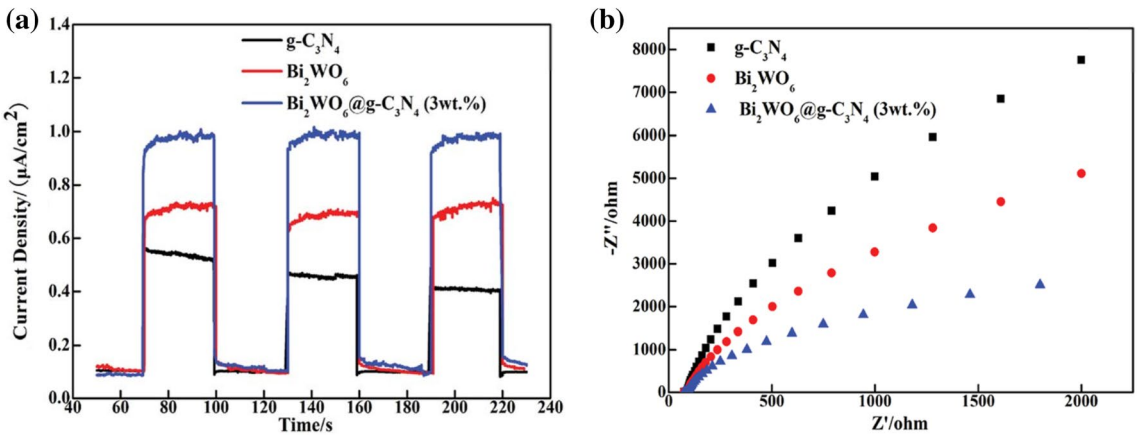

Fig. 15 **a** Transient photo-current under visible light irradiation and **b** Electrochemical impedance spectroscopy of g-C_3N_4, Bi_2WO_6 and Bi_2WO_6@g-C_3N_4. Reprinted from Ref. [64] Copyright 2015, with permission from Royal Society of Chemistry

pure ZnO, and the ZnO@g-C_3N_4 containing different content of g-C_3N_4 as illustrated in Fig. 16. Proposed mechanism for the promotion of the photo-electrochemical anti-corrosion performance of 304 stainless steel in ZnO@g-C_3N_4 is that the photo-induced holes in VB of ZnO are transferred to VB of g-C_3N_4 which then participate in the oxidation process on the surface of g-C_3N_4, while the photo-generated electrons at the CB of g-C_3N_4 are transferred to the CB of ZnO, and finally transferred to the 304 stainless steel through the conductive glass to achieve the metal cathodic protection under light irradiation. Importantly, heterojunction interface between g-C_3N_4 and ZnO indeed plays a vital role in the transmission of photo-generated electrons and holes. Using a similar mechanism with ZnO@g-C_3N_4, Sun et al. [51] fabricated In_2O_3@g-C_3N_4-3 wt% composite which exhibited the best photo-electrochemical anti-corrosion capability compared with its counterparts. Meanwhile, better photo-induced electron separation efficiency and resistance to recombination ability of photo-generated electron and hole pairs, lower photo-generated electron transfer resistance in In_2O_3@g-C_3N_4 3 wt% composite were proved by EIS, TPR as well.

3.4 Photo-catalytic reduction of CO_2

Photo-catalytic reduction of CO_2 is considered as one of the most promising technologies to relieve the greenhouse effect and energy crisis. The $LaPO_4$@*tube*g-C_3N_4 sample with core–shell structure synthesized by Li [58] had a significant improvement in photo-catalytic CO_2 reduction compared with $LaPO_4$ sample. As a reduction product, the yield of CO reaching 14.4/μmol/g/h was 8.07 and 10.36 times higher than that of pure tubular g-C_3N_4 and $LaPO_4$,

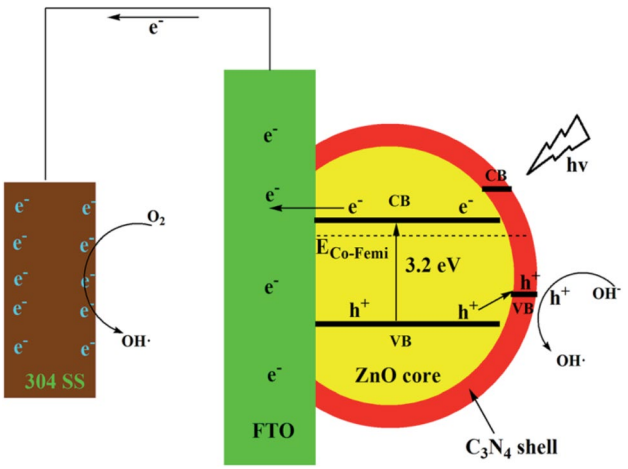

Fig. 16 Proposed mechanism for the promotion of the photo-electrochemical anti-corrosion performance for 304 stainless steel by 1 wt% g-C_3N_4/ZnO quasi-shell–core composite. Reprinted from Ref. [63] Copyright 2014, with permission from Royal Society of Chemistry

respectively. Moreover, the heterojunction interface between tubular g-C_3N_4 and $LaPO_4$ does not only significantly reduce the recombination rate of photo-generated electron and hole pairs and improve visible light absorption, but it also enhances photo-stability of $LaPO_4$@*tube*g-C_3N_4. After each reaction cycle, the catalyst was heated in a drying oven for 2 h to remove the possible residue such as CO. After 3 cycles of photo-catalytic experiments, the catalytic activity did not show the apparent reduction.

In fact, the number of applications in the photo-catalytic reduction of CO_2 based on the nanomaterial@g-C_3N_4 with core–shell structure is rather low in recent years. The complicated experimental process requiring pressure and temperature system and limited knowledge in the reduction of CO_2 may impede applications of nanomaterial@g-C_3N_4. Predictably, various nanomaterial@g-C_3N_4 in the photo-catalytic reduction of CO_2 will be further investigated in the future.

4 Summary

In summary, a number of g-C_3N_4-based core–shell nanocomposites have been explored and investigated in photo-catalysis and other related fields, which showed the improved performance when compared with bare g-C_3N_4 and nanocore. These results confirmed that the incorporation of g-C_3N_4 and the formation of core–shell structure could bring g-C_3N_4-based nanocomposites unique properties and promote enhanced performance. Compared with the common g-C_3N_4 supported photo-catalysts, the photo-catalysts with core–shell structure have the following good properties. Firstly, core–shell nanocomposites possessing larger contact area between core and shell are more beneficial to the formation of heterojunction, which can facilitate transmission and separation of photo-induced carriers and prolong the charge carrier lifetime, leading to higher catalytic activity (Fig. 15). Secondly, heterojunction interface between nanomaterial core and g-C_3N_4 shell can motivate more photo-generated protons or electrons and enhance absorption of visible light compared with single component due to photo-sensitization effect. (Fig. 12). Thirdly, nanomaterial@g-C_3N_4 with core–shell structure can prevent nanomaterial core from aggregation with each other, photo-corrosion, over oxidation–reduction and dissolution through isolation effect of the g-C_3N_4 shell (Fig. 14). Finally, ultrathin g-C_3N_4 shell (about 1 ~ 20 nm) in nanomaterial@g-C_3N_4 can speed up the transmission of photo-induced electrons.

Based on these obvious advantages, it is expected that g-C_3N_4-based core–shell nanocomposites will be a hot spot in the near future. Despite recent improvements in the preparation and application of g-C_3N_4-based core–shell nanocomposites, the studies in this field are still at the

primary stage and the understanding of charge generation and separation, control of charge transport between core and shell, the effects of interface properties of nanocomposites on chemisorption and photo-catalytic reaction, enhanced mechanisms of g-C_3N_4 modification are under investigation. Especially, the design and synthesis of g-C_3N_4-based core–shell nanocomposites with efficient optical absorption and separation of photo-generated electrons and holes remain a challenge. After reviewing and summarizing the related literatures, we can see that the nanocore is the most important factor for the construction of highly efficient photo-catalytic materials, which will have the significant influence on optical absorption, carrier generation, separation, transportation, and utilizations. Moreover, the suitable preparation strategy of g-C_3N_4-based core–shell nanocomposites can help to obtain ultrathin g-C_3N_4 nanosheets, good dispersion of g-C_3N_4 on the shell and strong interaction between nanocore and shell, which can enhance the photo-catalytic activity of nanocomposites. Thus, the basic requirements for nanocore to design efficient g-C_3N_4-based core–shell nanocomposites including the energy level, lattice structure, physical and chemical properties of nanocore and preparation method of nanocomposites are discussed briefly as below.

4.1 Energy level of nanocore

As is known to all, the photo-catalytic activity of nanocomposites depends greatly on energy band structure. Generally, overlapping band-structures of g-C_3N_4 and nanocore can favor the directional transfer and separation of photo-generated charges, and prolong the lifetime of electron–hole pairs, which can apparently improve the photo-catalytic performance of nanocomposites. According to the relationship of the energy level of g-C_3N_4 and nanocore semiconductor, there exist 6 possible overlapping band-structures as presented in Scheme 3 [102]. In the cases of Scheme 3a–c, the band gaps of nanocore are larger than that of g-C_3N_4 (~2.7 eV), while the band gap of nanocore shown in Scheme 3 (d), (e) and (f) are smaller than that of g-C_3N_4. There is no doubt that g-C_3N_4 is a visible light driven photo-catalyst, and responsive to the light with the wavelength of ~420 nm, which is nearly regarded

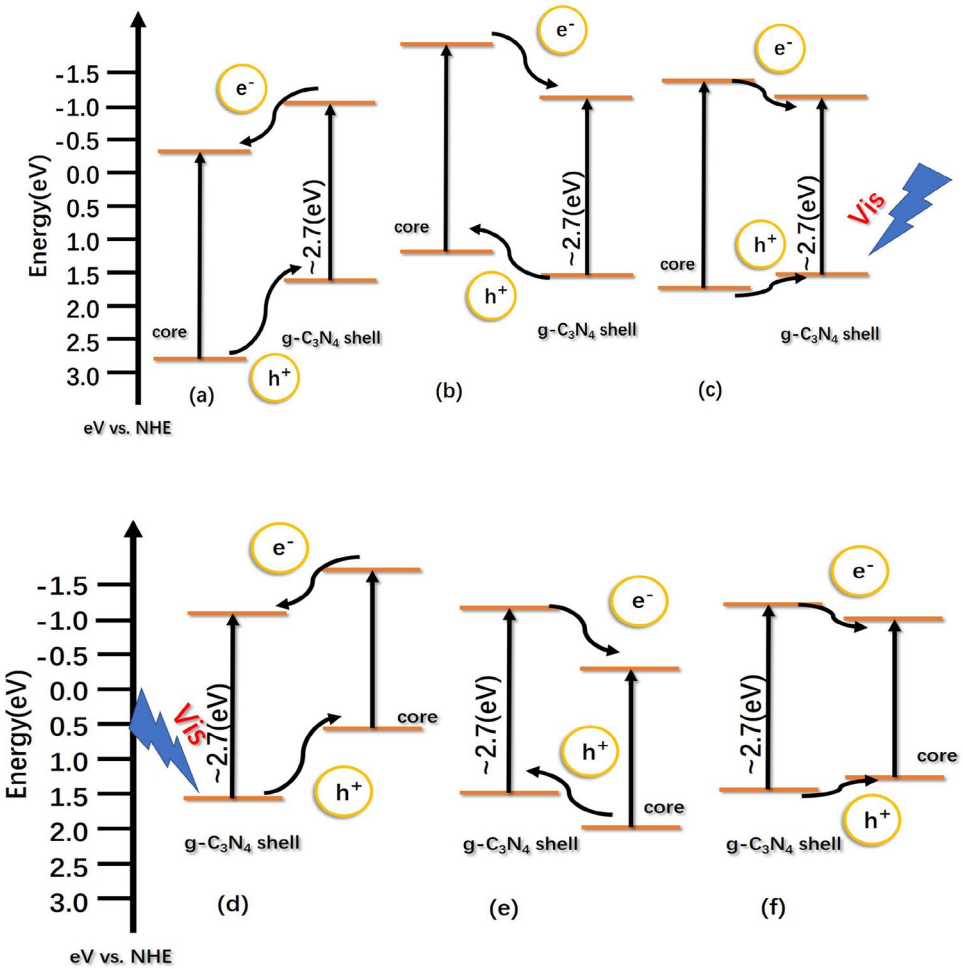

Scheme 3 Schematic illustration of electrons and holes transfer route in nanomaterial@g-C_3N_4 photo-catalysts with the different energy level of core and g-C_3N_4

as the watershed between visible light and ultraviolet light. Therefore, the nanocomposites of g-C_3N_4 and nanocore with band gap much larger than 2.7 eV are hard to exhibit good photo-activity under visible light for the energy band structure in Scheme 3 (a), (b) and (c) due to the weak visible light absorption. In contrast, the nanocomposites of g-C_3N_4 and nanocore with smaller band gap can show the improved photo-activity under visible light due to the increase of visible light absorption and more photo-generated electrons and holes. Overall, band match types as shown in Scheme 3d–f are likely superior to that in Scheme 3a–c.

When compared with the band structure in Scheme 3d–f, it can be found that in Scheme 3f both photo-generated electrons and holes in g-C_3N_4 will transfer to nanocore to form one-way accumulation. Theoretically, it is hard to reduce the recombination rate of photo-induced electron and hole pairs due to lack of isolation of photo-induced electrons and holes. As for band structures in Scheme 3d and e, the photo-generated electrons and holes can be transferred to nanocore or g-C_3N_4, respectively, and effectively separated owing to the formation of the heterojunction between nanocore and g-C_3N_4. Nevertheless, for band structure in Scheme 3d the photo-generated electrons are mainly accumulated in the CB of g-C_3N_4, and photo-generated holes are mainly collected in the VB of nanocore, and the situation is just opposite to band structure in Scheme 3e. Obviously, nanocomposites with band structures above as shown in Scheme 3d indeed have photo-generated electrons with stronger reducing power, and those with band structures above as shown in Scheme 3e can produce photo-generated holes with stronger oxidizing power. Therefore, the band match type in Scheme 3d is more likely to be valuable in the reduction of CO_2. While band match type in Scheme 3e is likely suitable to be used in pollutant degradation and photo-electrochemical anti-corrosion. As we all know, superoxide radicals, direct holes and hydroxyl radicals are active species for the photo-catalytic degradation, which can be produced in − 0.28 V and + 2.27 V vs. SHE at pH 7 respectively. Interestingly, it is also proposed recently that photo-induced electrons can be transferred to VB of shell g-C_3N_4 from the CB of nanocore to form a direct Z-scheme charge separation path as illustrated in Scheme 4 [96]. Subsequently, the photo-generated holes in the VB of nanocore with more positive potential than + 2.27 V can produce hydroxyl radicals. Thus, the energy level of nanocore in Scheme 3e can perform better photo-activity in pollutant degradation based on 2 possible mechanisms above. Concerning photo-electrochemical anti-corrosion, photo-induced electrons can transfer easily from shell to protected metal such as 304 stainless steel through nanocore in Scheme 3e connected with the conductive glass to achieve the metal cathodic protection under light irradiation as well [51, 63]. Additionally. When coupling with nanocore with CB of more negative than − 0.413 V (vs. SHE at pH 7, potential for H_2O reduction) [27] and − 0.61 V (vs. SHE at pH 7, potential for CO_2 reduction), the band match type in Scheme 3e is also effective for hydrogen production from water splitting and photo-catalytic CO_2 reduction.

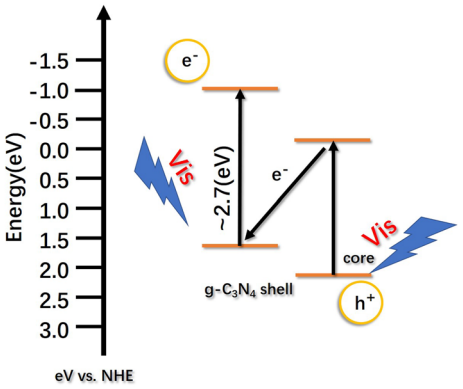

Scheme 4 Schematic illustration of electrons and holes transfer route (Z-scheme) in nanomaterial@g-C_3N_4 photo-catalysts for (e) type in Scheme 3

Thus, nanocore in Scheme 3 (e) can be regarded as the most efficient nanomaterial in applications above when coupling with g-C_3N_4 to form the core–shell structure.

4.2 Lattice match between g-C_3N_4 and nanocore

There are usually 2 peaks in XRD pattern of g-C_3N_4, a weak and broad peak usually at ~ 13.0° is related to the (100) crystal face of tris-triazine with the corresponding interlayer distance of ~ 0.681 nm. Another strong peak at ~ 27.5° is indexed to the (002) crystal face of stacking layered structure with an interplanar distance of ~ 0.324 nm [22, 103]. It is noteworthy that lattice characteristics of nanocore such as lattice spacing may play important roles in improving the photo-catalytic performance of nanocore@g-C_3N_4. Actually, It has been illustrated that the similar lattice characteristics such as atomic distance in the contact interface of both g-C_3N_4 and adjacent nanocore cannot only be conducive to synergetic effect as shown in Scheme 2 above [3, 56] but also possibly lead to faster photo-induced electrons transfer due to the decrease of electronic resistance. Predictably, that nanocore with the lattice spacing of ~ 0.324 nm or ~ 0.681 nm may be more suitable to combine with g-C_3N_4 to perform optimal photo-activity.

Furthermore, crystal face of photo-catalyst with higher activity often shows better photo-activity such as the crystal face (111) of octahedral Cu_2O exposed to the reaction system [73]. Therefore, crystal face exposed to the reaction system with better catalytic activity in nanocore also should be highlighted in the choice of nanocore.

Combination of the crystal face with high catalytic activity and similar lattice characteristics with g-C_3N_4 in

nanocore can be further investigated. In summary, it is an ideal way to take advantage of two strategies above simultaneously when designing nanocore@g-C_3N_4.

4.3 Physical and chemical properties of nanocore

Adsorption capacity in nanocore should be considered carefully as for some photo-catalytic applications such as photo-catalytic reduction of CO_2. As we all know, CO_2 belongs to acid gas, so basic nanocore or nanocore containing primary groups can perform better adsorption capacity [104], consequently better photo-activity can be predicted when using appropriate nanocore. Also, the certain morphology in nanocore such as nanorod, sphere, nanosheet can also be discussed. Nanosheet material can be promising nanocore to achieve the fast transfer of photo-generated electrons due to the fact that ultrathin nanosheets photo-catalyst's excellent catalytic activity has been proved [105] and then obtain improvement in photo-activity.

4.4 Preparation method of nanocomposites

Besides precursor wrapping method, physical adsorption is a comparatively better choice to prepare nanomaterial@g-C_3N_4 photo-catalysts due to its efficiency and easy controlling of the shell thickness by adjusting addition amount of g-C_3N_4. During the preparation of g-C_3N_4 nanosheets, the efficient acid treatment process can be taken into account. At the end of preparation, calcination operation for a short time with low temperature (~300 °C) can be considered as one step to form firm core–shell structure. Furthermore, there are two key points about the physical adsorption method. Firstly, mpg-C_3N_4 is the better choice regarding g-C_3N_4. This is because efficient exfoliation and the large surface area can bring the improvement in photo-activity. Meanwhile, the multi-dimensional structure of g-C_3N_4 is also conducive to the transmission of molecules or photo-induced electrons. Secondly, loading amount of g-C_3N_4 on the surface of nanocore may have an important influence on improving the catalyst's photo-activity [87, 106]. Too much or too little content of g-C_3N_4 could impair electrons transfer between the nanocore and the g-C_3N_4. While it can be seen from Table 1 that approximately 3–5 wt% content of g-C_3N_4 is appropriate addition amount in photo-catalyst. On the one hand, this is because totally enclosed shell may suppress the production of photo-generated electrons on the visible light driven nanocore due to the lack of irradiation. Consequently, it reduces the number of dominant reactive species in the redox reaction. On the other hand, the closed shell can prevent nanocore from contacting the reactant. Thus, redox products may be diminished drastically. For example, it is explained that too thick shell could suppress the transmission of electrons on the VB of Bi_2WO_6 to the surface of g-C_3N_4 and lead to the decrease in the number of superoxide radicals which can be regarded as the primary reactive species in photo-catalytic reduction. Meanwhile, recombination of photo-induced electron–hole pairs could be facilitated due to the dense shell. Therefore, photo-catalytic activity will decrease rapidly with the further increase of the g-C_3N_4 content. Similarly, too little content of g-C_3N_4 cannot support sufficient reactive species and intimate contact area which can be used to bridge for electrons transfer between nanocore and the g-C_3N_4. Thus, it is found that 3 ~ 5 wt% loading content for g-C_3N_4 will be more reasonable.

5 Conclusion and prospect

Photo-catalysis technology is indeed an ideal way to do with environmental pollution and energy shortages depending on suitable photo-catalyst. Fortunately, based on excellent physical and chemical stability, and appropriate electronic band structure and narrow bandgap with around 2.7 eV, which make g-C_3N_4 become visible light driven photo-catalyst and facilitate its applications in the reduction of CO_2 and H_2O as well as facile and safe preparation, the g-C_3N_4 is regarded as one of the most promising photo-catalyst recently. However, comparatively low photo-activity owing to its small surface area, the rapid recombination rate of photo-induced electron–hole pairs, low optical absorption in visible light and low electrical conductivity, high VB position limits further development of g-C_3N_4. In fact, graphitic carbon-nitride-based nanocomposites with core–shell structure can cope with deficiency of g-C_3N_4 regarding bandgap structure and fast recombination rate of electron–hole pairs by coupling suitable semi-conductor and g-C_3N_4. Apparently, the advantages of nanomaterial@g-C_3N_4 in improving photo-activity can be summarized as follows: Firstly, core–shell nanocomposites possessing larger contact area between core and shell are more beneficial to the formation of heterojunction, resulting in high transmission and separation of photo-induced carriers and prolonging the charge carrier lifetime; Secondly, heterojunction interface between nanomaterial core and g-C_3N_4 shell can motivate more photo-generated protons and enhance visible light response compared with single component due to photo-sensitization effect; Thirdly, core–shell structure of nanomaterial@g-C_3N_4 can prevent nanomaterial core from aggregation with each other, photo-corrosion, over oxidation–reduction and dissolution through isolation effect of g-C_3N_4 shell; Finally, ultrathin g-C_3N_4 shell (about 1 ~ 20 nm) in nanomaterial@g-C_3N_4 can accelerate the transmission of photo-induced electrons. Additionally, influence factors on the photo-catalytic performance of nanomaterial@g-C_3N_4 can be attributed to lattice match and energy level in nanocore, the preparation

method of nanocomposites including modification of g-C_3N_4 nanosheets as well as physical and chemical properties of nanocore.

Based on fantastic physicochemical stability and optical properties of g-C_3N_4 as well as efficient photo-electronic transportation as a result of the formation of the core–shell structure, the prospects of novel nanomaterial@g-C_3N_4 can be predicted regarding 3 aspects. Firstly, functional materials in terms of g-C_3N_4 or nanocore will be further optimized. For instance, nanomaterial@g-C_3N_4 photo-catalysts containing 3 components or more than 3 components [107] may achieve a longer lifetime of photo-generated electron–hole pairs (e.g. (a-TiO_2@c-TiO_2)@g-C_3N_4 [75], $Ni(OH)_2$-CdS@g-C_3N_4 [91]) compared with the core structure of photo-catalyst with binary components. Also, the more abundant functional shell of g-C_3N_4 nanosheets such as non-metallic element doped g-C_3N_4 or morphology modification remains to be explored. Predictably, the more complicated functional nanomaterial@g-C_3N_4 photo-catalysts will pave the novel avenue in improving photo-activity. Secondly, the preparation strategy of nanomaterial@g-C_3N_4 will be further improved, which will become simpler and less-expensive. More importantly, the more stable core–shell structure is rather essential via optimizing preparation strategy. Thirdly, the applications in the photo-catalysis or photo-electricity field will be further expanded due to the excellent photo-catalytic activity of nanomaterial@g-C_3N_4. In fact, there still is the lack of sufficient applications in the photo-catalytic reduction of CO_2 which is considered as the promising way to resolve the environmental pollution and the shortage of fossil energy based on the nanomaterial@g-C_3N_4. It is believed that the nanomaterial@g-C_3N_4 will continue playing a significantly important role in the future in the photo-electric stage.

Acknowledgements We gratefully acknowledge the financial supports from the National Natural Science Foundation of China (Nos. 21276190 and 20806059).

References

1. W. Jiang, W. Luo, J. Wang, M. Zhang, Y. Zhu, J. Photochem. Photobiol. C **28**, 87–115 (2016)
2. T. Inoue, A. Fujishima, S. Konishi, K. Honda, Nature. **277**, 637–638 (1979)
3. D. Chen, K. Wang, D. Xiang, R. Zong, W. Yao, Y. Zhu, Appl. Catal. B Environ. **147**, 554–561 (2014)
4. S.J. Hong, S. Lee, J.S. Jang, J.S. Lee, Energy Environ. Sci. **4**, 1781 (2011)
5. J. Yu, Y. Hai, M. Jaroniec, J. Colloid Interface Sci. **357**, 223–228 (2011)
6. D. Barreca, P. Fornasiero, A. Gasparotto, V. Gombac, C. Maccato, T. Montini, E. Tondello, ChemSusChem. **2**, 230–233 (2009)
7. P.-W. Pan, Y.-W. Chen, Catal. Commun. **8**, 1546–1549 (2007)
8. S. Ouyang, H. Tong, N. Umezawa, J. Cao, P. Li, Y. Bi, Y. Zhang, J. Ye, J. Am. Chem. Soc. **134**, 1974–1977 (2012)
9. Y. Yamada, K. Yano, D. Hong, S. Fukuzumi, Phys. Chem. Chem. Phys. **14**, 5753–5760 (2012)
10. J. Zhang, S. Liu, J. Yu, M. Jaroniec, J. Mater. Chem. **21**, 14655 (2011)
11. Q. Li, B. Guo, J. Yu, J. Ran, B. Zhang, H. Yan, J.R. Gong, J. Am. Chem. Soc. **133**, 10878–10884 (2011)
12. M. Abou Asi, L. Zhu, C. He, V.K. Sharma, D. Shu, S. Li, J. Yang, Y. Xiong, Catal. Today. **216**, 268–275 (2013)
13. N. Ahmed, M. Morikawa, Y. Izumi, Catal Today. **185**, 263–269 (2012)
14. M. Morikawa, N. Ahmed, Y. Yoshida, Y. Izumi, Appl. Catal. B Environ. **144**, 561–569 (2014)
15. P. Mazierski, M. Nischk, M. Gołkowska, W. Lisowski, M. Gazda, M.J. Winiarski, T. Klimczuk, A. Zaleska-Medynska, Appl. Catal. B Environ. **196**, 77–88 (2016)
16. G. Yang, Z. Jiang, H. Shi, T. Xiao, Z. Yan, J. Mater. Chem. **20**, 5301 (2010)
17. J. Wang, T. Tsuzuki, B. Tang, X. Hou, L. Sun, X. Wang, ACS Appl. Mater. Interfaces. **4**, 3084–3090 (2012)
18. F. Xu, Y. Yuan, H. Han, D. Wu, Z. Gao, K. Jiang, CrystEngComm. **14**, 3615 (2012)
19. S. Kumar, A. Baruah, S. Tonda, B. Kumar, V. Shanker, B. Sreedhar, Nanoscale. **6**, 4830–4842 (2014)
20. R. Abe, J. Photochem. Photobiol. C **11**, 179–209 (2010)
21. X. Fang, J. Song, T. Pu, C. Wang, C. Yin, J. Wang, S. Kang, H. Shi, Y. Zuo, Y. Wang, L. Cui, Int. J. Hydrog. Energy. **42**, 28183–28192 (2017)
22. X. Wang, K. Maeda, A. Thomas, K. Takanabe, G. Xin, J.M. Carlsson, K. Domen, M. Antonietti, Nat. Mater. **8**, 76–80 (2009)
23. S. Cao, J. Yu, J. Phys. Chem. Lett. **5**, 2101–2107 (2014)
24. P. Niu, L. Zhang, G. Liu, H.-M. Cheng, Adv. Funct. Mater. **22**, 4763–4770 (2012)
25. J. Mao, T. Peng, X. Zhang, K. Li, L. Ye, L. Zan, Catal. Sci. Technol. **3**, 1253 (2013)
26. K. Maeda, X. Wang, Y. Nishihara, D. Lu, M. Antonietti, K. Domen, Phys. Chem. **113**, 4940–4947 (2009)
27. A. Fujishima, X. Zhang, C. R. Chim. **9**, 750–760 (2006)
28. S. Cao, J. Low, J. Yu, M. Jaroniec, Adv. Mater. **27**, 2150–2176 (2015)
29. S.C. Yan, Z.S. Li, Z.G. Zou, Langmuir. **26**, 3894–3901 (2010)
30. L. Ye, J. Liu, Z. Jiang, T. Peng, L. Zan, Appl. Catal. B Environ. **142–143**, 1–7 (2013)
31. J. Sun, J. Xu, A. Grafmueller, X. Huang, C. Liedel, G. Algara-Siller, M. Willinger, C. Yang, Y. Fu, X. Wang, M. Shalom, Appl. Catal. B Environ. **205**, 1–10 (2017)
32. L. Huang, H. Xu, R. Zhang, X. Cheng, J. Xia, Y. Xu, H. Li, Appl. Surf. Sci. **283**, 25–32 (2013)
33. Y. Hong, Y. Jiang, C. Li, W. Fan, X. Yan, M. Yan, W. Shi, Appl. Catal. B Environ. **180**, 663–673 (2016)
34. H. Shen, X. Zhao, L. Duan, R. Liu, H. Li, Mater. Sci. Eng. B. **218**, 23–30 (2017)
35. Y. Hou, Y. Gan, Z. Yu, X. Chen, L. Qian, B. Zhang, L. Huang, J. Huang, J. Power Sour. **371**, 26–34 (2017)
36. J. Lin, Z. Pan, X. Wang, ACS Sustain. Chem. Eng. **2**, 353–358 (2014)
37. J. Zhang, M. Zhang, R.Q. Sun, X. Wang, Angew Chem. Int. Ed. Engl. **51**, 10145–10149 (2012)
38. Q. Huang, J. Yu, S. Cao, C. Cui, B. Cheng, Appl. Surf. Sci. **358**, 350–355 (2015)
39. G. Zhang, J. Zhang, M. Zhang, X. Wang, J. Mater. Chem. **22**, 8083 (2012)
40. Z. Zhao, Y. Sun, F. Dong, Nanoscale. **7**, 15–37 (2015)
41. K. Maeda, R. Kuriki, M. Zhang, X. Wang, O. Ishitani, J. Mater. Chem. A. **2**, 15146–15151 (2014)

42. Y. Zheng, L. Lin, B. Wang, X. Wang, Angew Chem Int. Ed. Engl. **54**, 12868–12884 (2015)
43. M. Zhang, X. Bai, D. Liu, J. Wang, Y. Zhu, Appl. Catal. B Environ. **164**, 77–81 (2015)
44. L. Zhao, L. Zhang, H. Lin, Q. Nong, M. Cui, Y. Wu, Y. He, J. Hazardous Mater. **299**, 333–342 (2015)
45. Y. Sun, J. Jiang, Y. Liu, S. Wu, J. Zou, Appl. Surf. Sci. **430**, 362–370 (2018)
46. X. Bai, R. Zong, C. Li, D. Liu, Y. Liu, Y. Zhu, Appl. Catal. B Environ. **147**, 82–91 (2014)
47. H. Yan, H. Yang, J. Alloys Compd. **509**, L26–L29 (2011)
48. R.C. Pawar, Y. Son, J. Kim, S.H. Ahn, C.S. Lee, Curr. Appl. Phys. **16**, 101–108 (2016)
49. Q. Wang, Y. Shi, Z. Du, J. He, J. Zhong, L. Zhao, H. She, G. Liu, B. Su, Eur. J. Inorgan. Chem. **2015**, 4108–4115 (2015)
50. F. Di Quarto, C. Sunseri, S. Piazza, M.C. Romano, Phys. Chem. **101**, 2519–2525 (1997)
51. M. Sun, Z. Chen, Y. Bu, J. Alloys Compd. **618**, 734–741 (2015)
52. S. Ye, R. Wang, M.-Z. Wu, Y.-P. Yuan, Appl. Surf. Sci. **358**, 15–27 (2015)
53. J. Tian, Q. Liu, A.M. Asiri, A.O. Al-Youbi, X. Sun, Anal. Chem. **85**, 5595–5599 (2013)
54. N. Cheng, J. Tian, Q. Liu, C. Ge, A.H. Qusti, A.M. Asiri, A.O. Al-Youbi, X. Sun, ACS Appl. Mater. Interfaces. **5**, 6815–6819 (2013)
55. J. Tian, Q. Liu, C. Ge, Z. Xing, A.M. Asiri, A.O. Al-Youbi, X. Sun, Nanoscale. **5**, 8921–8924 (2013)
56. C. Pan, J. Xu, Y. Wang, D. Li, Y. Zhu, Adv. Funct. Mater. **22**, 1518–1524 (2012)
57. S. Duan, G. Han, Y. Su, X. Zhang, Y. Liu, X. Wu, B. Li, Langmuir. **32**, 6272–6281 (2016)
58. M. Li, L. Zhang, X. Fan, M. Wu, M. Wang, R. Cheng, L. Zhang, H. Yao, J. Shi, Appl. Catal. B Environ. **201**, 629–635 (2017)
59. L. Liu, Y. Qi, J. Hu, W. An, S. Lin, Y. Liang, W. Cui, Mater. Lett. **158**, 278–281 (2015)
60. Y. Li, X. Wei, H. Li, R. Wang, J. Feng, H. Yun, A. Zhou, RSC Adv. **5**, 14074–14080 (2015)
61. L. Liu, Y. Qi, J. Yang, W. Cui, X. Li, Z. Zhang, Appl. Surf. Sci. **358**, 319–327 (2015)
62. R. Chen, J. Zhang, Y. Wang, X. Chen, J.A. Zapien, C.S. Lee, Nanoscale. **7**, 17299–17305 (2015)
63. Y. Bu, Z. Chen, RSC Adv. **4**, 45397–45406 (2014)
64. L. Liu, Y. Qi, J. Lu, S. Lin, W. An, J. Hu, Y. Liang, W. Cui, RSC Adv. **5**, 99339–99346 (2015)
65. L. Liu, Y. Qi, J. Lu, S. Lin, W. An, Y. Liang, W. Cui, Appl. Catal. B Environ. **183**, 133–141 (2016)
66. Y. Yao, F. Lu, Y. Zhu, F. Wei, X. Liu, C. Lian, S. Wang, J. Hazard. Mater. **297**, 224–233 (2015)
67. J. Zhang, Y. Wang, J. Jin, J. Zhang, Z. Lin, F. Huang, J. Yu, ACS Appl. Mater. Interfaces. **5**, 10317–10324 (2013)
68. X. Zhang, X. Xie, H. Wang, J. Zhang, B. Pan, Y. Xie, J. Am. Chem. Soc. **135**, 18–21 (2013)
69. L. Shi, K. Chang, H. Zhang, X. Hai, L. Yang, T. Wang, J. Ye, Small. **12**, 4431–4439 (2016)
70. W. Chen, T.Y. Liu, T. Huang, X.H. Liu, X.J. Yang, Nanoscale. **8**, 3711–3719 (2016)
71. Z. Xing, Y. Chen, C. Liu, J. Yang, J. Xu, Y. Situ, H. Huang, J. Alloys Compd. **708**, 853–861 (2017)
72. B. Lin, H. An, X. Yan, T. Zhang, J. Wei, G. Yang, Appl. Catal. B Environ. **210**, 173–183 (2017)
73. L. Liu, Y. Qi, J. Hu, Y. Liang, W. Cui, Appl. Surf. Sci. **351**, 1146–1154 (2015)
74. L. Ma, G. Wang, C. Jiang, H. Bao, Q. Xu, Appl. Surf. Sci. **430**, 263–272 (2018)
75. A.P. Singh, P. Arora, S. Basu, B.R. Mehta, Int. J. Hydrog. Energy. **41**, 5617–5628 (2016)
76. L. Wang, F. Zhao, Q. Han, C. Hu, L. Lv, N. Chen, L. Qu, Nanoscale. **7**, 9694–9702 (2015)
77. S. Gholizadeh Khasevani, N. Mohaghegh, M.R. Gholami, New J. Chem. **41**, 10390–10396 (2017)
78. T.J. Park, R.C. Pawar, S. Kang, C.S. Lee, RSC Adv. **6**, 89944–89952 (2016)
79. B. Lin, C. Xue, X. Yan, G. Yang, G. Yang, B. Yang, Appl. Surf. Sci. **357**, 346–355 (2015)
80. Y. Zhang, R. Wen, D. Guo, H. Guo, J. Chen, Z. Zheng, Appl. Organomet. Chem. **30**, 160–166 (2016)
81. X. Wang, S. Blechert, M. Antonietti, ACS Catal. **2**, 1596–1606 (2012)
82. J. Liu, J. Huang, H. Zhou, M. Antonietti, ACS Appl. Mater. Interfaces. **6**, 8434–8440 (2014)
83. J. Huang, M. Antonietti, J. Liu, J. Mater. Chem. A. **2**, 7686 (2014)
84. S. Kang, H. Qin, L. Zhang, Y. Huang, X. Bai, X. Li, D. Sun, Y. Wang, L. Cui, Sci Rep. **7**, 44338 (2017)
85. Z. Chen, G. Ma, Z. Chen, Y. Zhang, Z. Zhang, J. Gao, Q. Meng, M. Yuan, X. Wang, G. Liu, Zhou, J.-m. Appl. Surf. Sci. **396**, 609–615 (2017)
86. J. Zhou, M. Zhang, Y. Zhu, Phys. Chem. Chem. Phys. **17**, 3647–3652 (2015)
87. X. Fan, T. Wang, B. Gao, H. Gong, H. Xue, H. Guo, L. Song, W. Xia, X. Huang, J. He, Langmuir. **32**, 13322–13332 (2016)
88. Y. Zou, J.-W. Shi, D. Ma, Z. Fan, L. Lu, C. Niu, Chem. Eng. J. **322**, 435–444 (2017)
89. J. Zhou, M. Zhang, Y. Zhu, Phys. Chem. Chem. Phys. **16**, 17627–17633 (2014)
90. L. Liu, P. Hu, W. Cui, X. Li, Z. Zhang, Int. J. Hydrog. Energy. **42**, 17435–17445 (2017)
91. Z. Yan, Z. Sun, X. Liu, H. Jia, P. Du, Nanoscale. **8**, 4748–4756 (2016)
92. P. Wang, N. Lu, Y. Su, N. Liu, H. Yu, J. Li, Y. Wu, Appl. Surf. Sci. **423**, 197–204 (2017)
93. M. Ning, Z. Chen, L. Li, Q. Meng, Z. Chen, Y. Zhang, M. Jin, Z. Zhang, M. Yuan, X. Wang, G. Zhou, Electrochem. Commun. **87**, 13–17 (2018)
94. L. Ma, H. Fan, K. Fu, S. Lei, Q. Hu, H. Huang, G. He, ACS Sustain. Chem. Eng. **5**, 7093–7103 (2017)
95. D. Tang, G. Zhang, Appl. Surf. Sci. **391**, 415–422 (2017)
96. Y. Hong, C. Li, B. Yin, D. Li, Z. Zhang, B. Mao, W. Fan, W. Gu, W. Shi, Chem. Eng. J. **338**, 137–146 (2018)
97. Z. Zhang, M. Wang, W. Cui, H. Sui, RSC Adv. **7**, 8167–8177 (2017)
98. C. Liu, C. Zhang, J. Wang, Q. Xu, X. Chen, C. Wang, X. Xi, W. Hou, Mater. Lett. **217**, 235–238 (2018)
99. Y. He, L. Zhang, B. Teng, M. Fan, Environ. Sci. Technol. **49**, 649–656 (2015)
100. W. Yu, D. Xu, T. Peng, J. Mater. Chem. A. **3**, 19936–19947 (2015)
101. J. Hao, S. Zhang, F. Ren, Z. Wang, J. Lei, X. Wang, T. Cheng, L. Li, J. Colloid Interface Sci. **508**, 419–425 (2017)
102. S. Liu, L. Ma, H. Zhang, C. Ma, Mater. Sci. Eng. B. **207**, 33–38 (2016)
103. Y. Huang, Y. Wang, Y. Bi, J. Jin, M.F. Ehsan, M. Fu, T. He, RSC Adv. **5**, 33254–33261 (2015)
104. C. Xin, M. Hu, K. Wang, X. Wang, Langmuir. **33**, 6667–6676 (2017)
105. S. Zhu, S. Liang, J. Bi, M. Liu, L. Zhou, L. Wu, X. Wang, Green Chem. **18**, 1355–1363 (2016)
106. Y. Wang, W. Yang, X. Chen, J. Wang, Y. Zhu, Appl. Catal. B Environ. **220**, 337–347 (2018)
107. D. Lu, H. Wang, Q. Shen, K.K. Kondamareddy, D. Neena, J. Phys. Chem. Solids. **106**, 76–81 (2017)